# UNMANNED AERIAL VEHICLE REMOTE SENSING OF SOIL MOISTURE WITH I-BAND SIGNALS OF OPPORTUNITY

A Thesis

Submitted to the Faculty

of

Purdue University

by

Jared D. Covert

In Partial Fulfillment of the

Requirements for the Degree

of

Master of Science

May 2020

Purdue University

West Lafayette, Indiana

# THE PURDUE UNIVERSITY GRADUATE SCHOOL
# STATEMENT OF THESIS APPROVAL

Dr. James L. Garrison, Chair

School of Aeronautics and Astronautics

Dr. David A. Spencer

School of Aeronautics and Astronautics

Dr. Dara Entekhabi

Massachusetts Institute of Technology

**Approved by:**

Dr. Gregory Blaisdell

Associate Head for the Graduate Program

To my parents, Doug and Chris Covert, and my brother, Justin Covert, for without their love and support I would never have made it this far. And to COVID-19, for allowing this opportunity to show that progress shall always continue in the face of adversity.

"We did not seek nor did we provoke an assault on our freedom and our way of life. We did not expect nor did we invite a confrontation with evil. Yet the true measure of a people's strength is how they rise to master that moment when it does arrive."

- President Josiah Bartlet, *The West Wing*

# ACKNOWLEDGMENTS

I would like to thank all of my labmates for their assistance with my work and for the great friendships we have made: Ben, Abi, Priyankar, Harris, Seho, Archie, Eric, and Sidd. Ben is a lifesaver and great friend and engineer. I will miss the sarcastic explanations of how EE works. Special recognition to my former SURF, Eric, for his specific work on this project. I will greatly miss the time we spent together in and out of the lab.

Thank you to all of my friends, whether Purdue, Academy, or Ohio, for helping me stay sane throughout all of the ups and downs. I couldn't have done it without you all.

Lastly, a large thank you to the U.S. Air Force and the Purdue Military Research Initiative for giving me the opportunity to attend graduate school. Without the work of Dave Hankins and Dr. Eric Dietz, none of us military folk would be here.

TABLE OF CONTENTS

Page

# LIST OF TABLES

# LIST OF FIGURES

Figure Page

# SYMBOLS

| | |
|---|---|
| $t$ | Time |
| $E$ | Electric field |
| $\omega$ | Frequency |
| $\theta$ | Angle of Incidence |
| $\lambda$ | Wavelength |
| $\sigma_z$ | RMS Surface Height Standard Deviation |
| $a$ | Semi-major Axis |
| $b$ | Semi-minor Axis |
| $n$ | Refractive Index |
| $D_{TS}$ | Distance between Transmitter and Specular Point |
| $D_{RS}$ | Distance between Receiver and Specular Point |
| $h$ | Receiver Height |
| $\epsilon$ | Dielectric Constant |
| $\rho$ | Fresnel Reflection Coefficient |
| $\Gamma$ | Reflectivity |
| $C_D$ | Direct Signal Power |
| $C_R$ | Reflected Signal Power |
| $m_v$ | Volumetric Soil Moisture |
| $X_D$ | Direct Signal |
| $X_R$ | Reflected Signal |
| $G_{AS}(\theta_{DS})$ | Sky Antenna Gain of Direct Signal |
| $G_{AS}(\theta_{RS})$ | Sky Antenna Gain of Reflected Signal |
| $G_{AE}(\theta_{DE})$ | Earth Antenna Gain of Direct Signal |
| $G_{AE}(\theta_{RE})$ | Earth Antenna Gain of Reflected Signal |
| $X_T$ | Transmitted Signal |

| | |
|---|---|
| $C$ | Signal Power |
| $s(t)$ | Signal Modulation |
| $\omega_c$ | Carrier Frequency |
| $\phi_D$ | Direct Signal Phase Shift |
| $\phi_R$ | Reflected Signal Phase Shift |
| $\tau$ | Time Delay |
| $\tau_D$ | Direct Signal Time Delay |
| $\tau_R$ | Reflected Signal Time Delay |
| $\tau_{RD}$ | Time Delay between Direct and Reflected Signal |
| $\omega_{Dop}$ | Doppler Shift Frequency |
| $\omega_I$ | Intermediate Frequency |
| $d$ | Path Delay |
| $c$ | Speed of Light |
| $R_{11}(\tau)$ | Time Domain Autocorrelation |
| $R_{12}(\tau)$ | Time Domain Cross Correlation |
| $T_I$ | Integration Time |
| $P$ | Power |
| $\eta_1$ | System 1 Noise |
| $\eta_2$ | System 2 Noise |
| $\eta_{Cold}$ | Cold Load Noise |
| $\eta_{Ref}$ | Reference Load Noise |
| $\eta_{Dio}$ | Noise Diode Noise |
| $\eta_{AS}$ | Sky Antenna Noise |
| $\eta_{AE}$ | Earth Antenna Noise |
| $T_1$ | System 1 Noise Temperature |
| $T_2$ | System 2 Noise Temperature |
| $T_{Cold}$ | Cold Load Noise Temperature |
| $T_{Ref}$ | Reference Load Noise Temperature |
| $T_{Dio}$ | Noise Diode Noise Temperature |

| | |
|---|---|
| $T_{AS}$ | Sky Antenna Noise Temperature |
| $T_{AE}$ | Earth Antenna Noise Temperature |
| $K$ | Boltzmann Constant |
| $B$ | Bandwidth |
| $N_0$ | Power Spectral Noise Density |
| $G_1$ | System 1 Gain |
| $G_2$ | System 2 Gain |
| $P_t$ | Transmitter Power |
| $G_t$ | Transmitter Gain |
| $L_0$ | Path Loss |
| $L_A$ | Atmospheric Loss |
| $L_P$ | Polarization Loss |
| $G_r$ | Receiver Gain |
| $\sigma$ | Stefan-Boltzmann Constant |
| $F$ | Noise Factor |
| $AZ$ | Azimuth |
| $EL$ | Elevation Angle |
| $SR$ | Slant Range |

# ABSTRACT

Covert, Jared D. MS, Purdue University, May 2020. Unmanned Aerial Vehicle Remote Sensing of Soil Moisture with I-Band Signals of Opportunity. Major Professor: James L. Garrison.

Measurements of root zone soil moisture play large roles in our understanding of the water cycle, weather, climate, land-heat exchanges, drought forecasting, and agriculture. Current measurements are made using a combination of ground-based sampling and active and passive microwave remote sensing. Signals of Opportunity (SoOp) has emerged as a promising method for sensing soil moisture, using satellite communication signals to make bi-static reflectometry measurements. The current combination of ground and satellite-based measurements for soil moisture results in a gap of useful spatial and temporal resolutions, as well as limited soil penetration depth. This thesis developed and constructed an Unmanned Aerial Vehicle (UAV) mountable, I-band SoOp instrument with calibration capabilities, along with supporting specular point mapping and mission planning software. This work advances the creation of a compact, mobile, root zone soil moisture (RZSM) remote sensing system.

# 1. INTRODUCTION

## 1.1 Why Soil Moisture

According to the *Encyclopedia of Climate and Weather*, soil moisture holds approximately five one-hundredths of a percent of the Earth's total freshwater content [1]. While surface and sub-surface soil moisture may only represent a figurative drop of the Earth's overall water cycle, the importance of soil moisture and its impacts cannot be overlooked. Both the World Meteorological Organization and NASA have emphasized the importance of soil moisture in better understanding Earth's global processes, with the WMO calling it an "essential climate variable" [2] [3]. In addition, soil moisture is either directly mentioned or related to answering at least four of the "Societal or Science Questions/Goals" from the 2017 NASA Earth Observation Decadal Survey [4]. Of particular interest is the first meter of soil where plants obtain water, known as root zone soil moisture (RZSM).

Soil moisture plays a role in the modeling of aspects of the global water and climate cycles. *Carrera et al.* found in 2017 that assimilated remote sensing observations for soil moisture, rather than physical samples, improved weather forecasting models for North America [5]. Likewise, numerous studies have included or commented on the role soil moisture plays in regulating the Earth's land-heat exchange, which itself directly influences processes such as cloud formation and precipitation [6] [7]. Agriculture and biomass growth also depend on soil moisture. Soil moisture is directly connected to biomass growth, and NOAA estimates that biomass helps to remove up to 20% of the $CO_2$ from fossil fuels [8]. Models for land inundation and drought can be improved with soil moisture measurements, as in *Bolten et al.* who used soil moisture to assist in forecasting drought for agriculture in 2010 [9].

## 1.2 Manual/Ground Based Soil Moisture Techniques

Traditionally, soil moisture measurements relied on the taking of physical samples of soil to measure the water content. This method involves weighing a sample of soil before and after drying. The difference in weight allows the mass of water removed from the soil and thus the original soil moisture content to be calculated. The soil density must be known for this process. Soil moisture measurements can also be made using probes or ground stations. Electrical sensors inside the probe or station allow for soil moisture to be estimated based off of a variety of the soil's properties, such as impedance or capacitance.

Both types of measurements come with a limitation: spatially, they only represent point measurements. Studies, such as *Hawley et al.* in 1983, have shown that soil moisture can vary drastically across a given area depending on soil makeup and topography, which makes point measurements relatively impractical for areas like agriculture fields or watersheds [10]. Temporally, someone must physically take a sample every time a measurement is wanted. Even with automated systems or probes, periodic hand calibrations are still required. To allow for better measurements, spatially and temporally, remotely sensed observations must be used.

## 1.3 Microwave Remote Sensing for Soil Moisture

Microwave remote sensing is based on the detection of radiation being emitted or reflected by an object. Detecting emmisions is known as passive remote sensing whereas detecting radiation that is broadcast at an object is known as active remote sensing. A blackbody is an idealized object that absorbs all electromagnetic radiation in its direction, in addition to emitting electromagnetic radiation. Because nothing in existence is a true blackbody, the radiation an object gives off can be compared to that of a blackbody at the same temperature using Planck's Law. The ratio between the two is emissivity. In turn, various physical properties can be inferred from emissivity, including soil moisture. The Earth's atmosphere generally acts as a shield against

radiation, attenuating most incoming electromagnetic radiation except for that in the optical and radio/microwave regions.

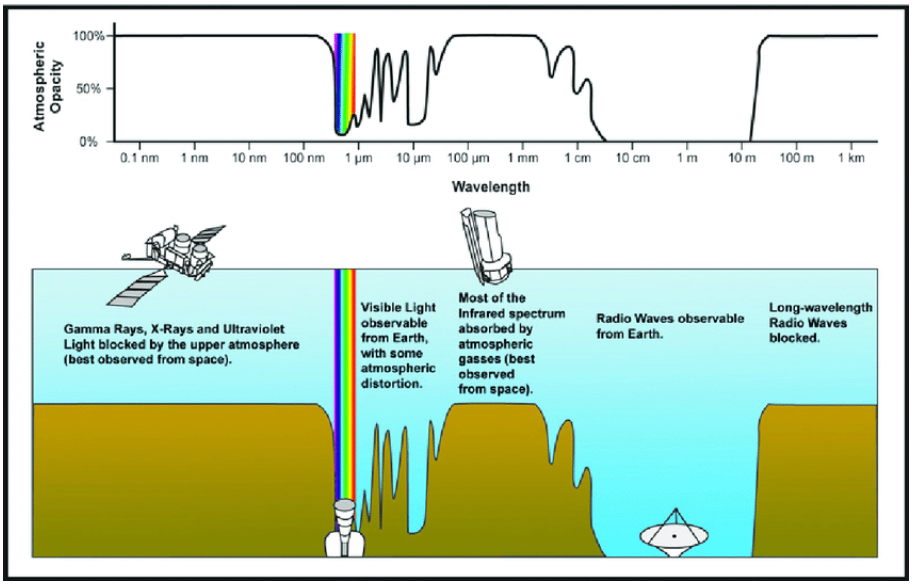


Figure 1.1.: Atmospheric Opacity vs. Wavelength [11]

As such, soil moisture is typically remote sensed using microwaves, which is the portion of the electromagnetic spectrum with a frequency of approximately 130 MHz to 300 GHz and wavelengths of three meters to one millimeter .

One active method used for estimating soil moisture is based off of a property known as reflectivity. Reflectivity is the ratio between the power of a signal or radiated wave that is reflected back when that wave strikes an object. This reflection can differ based on the dielectric properties of the interface. Water has a very high permittivity, whereas air does not. Because of this, water content of soil has a large impact on the dielectric properties of soil. As soil moisture increases, so does reflectivity. Using microwaves, this property can be exploited to find reflectivity, and from reflectivity infer soil moisture content.

Soil moisture remote sensing has its roots in missions from the 1970's, 80's, and 90's, which examined the use of passive microwave radiometers to observe soil moisture. More recently, NASA launched the L-band (1-2 GHz) Soil Moisture Active

Passive (SMAP) mission in 2015 with a goal of providing global observations of soil moisture and freeze-thaw to improve models for water, energy, and carbon [12]. ESA launched the C-band (4-8 GHz) Sentinel and X-band (8-12 GHz) SMOS missions in 2015 and 2009, respectively, to support soil moisture remote sensing. [13] [14]. In the late 1990s and early 2000's, research expanded in using GPS signals in a bistatic configuration for the remote sensing of various properties, such as altimetry and soil moisture [15] [16]. This form of remote sensing has come to be known as Global Navigation Satellite System Reflectometry or GNSS-R. Numerous tower-based experiments have proven the use of GNSS-R for soil moisture [16]. In 2016, the Cyclone Global Navigation Satellite System, or CYGNSS, was launched to conduct GNSS-R for hurricane forecasting. Recent research has been conducted showing the applicability of CYGNSS for soil moisture and other land applications [17] [18] [19].

Unfortunately, GNSS-R comes with limitations of its own. The temporal resolution of space-borne missions is still often on the order of days, which can be too long for certain applications such as land inundation. Satellites have spatial resolutions on the order of tens of kilometers, whereas tower experiments usually have spatial resolutions of a few square feet or meters. This results in a gap of data between the two for areas the size of a few fields or small farm. Finally, L-band and C-band based systems can only penetrate the first few centimeters of soil. Root zone soil mositure ,where plants obtain water, can extend to a meter beneath the surface. As a result, different methods and frequencies are needed to fill these gaps.

### 1.4 Signals of Opportunity

Signals of Opportunity (SoOp) is a bistatic remote sensing method that focuses on building a receiver to collect signals already being broadcast by communication systems; hence the term "Signals of Opportunity". It works in a similar fashion to GNSS-R but takes advantage of signals in other than frequency bands. A SoOp instrument uses both a direct and reflected signal to estimate properties like reflectivity.

The use of SoOp for remote sensing purposes was first conducted in 2009, which showed that measurements using L, S, and Ku-Band signals could be used for wave height measurements and ocean altimetry [20]. Further SoOp work in coastal altimetry using broadband DirecTV (K and Ku-band) signals showed a measurement precision of 4-6 centimeters [21]. An airborne RZSM instrument known as SoOp-AD was created and flown in 2016 over a lake in Oklahoma. It showed high reflectivity measurements over water as opposed to land using both P and S-bands [22]. Multiple tower experiments have also been conducted, such as those in 2017 and 2018 using a 106 ft. tall tower to measure soil moisture over the corn growth cycle of an agricultural research center in Indiana. [23].

Signals of Opportunity offers numerous benefits over that of a traditional spacecraft/remote sensing instrument because of its use of existing communication signals. The biggest advantage being that, unlike systems which use their own active transmitter, signal allocation is not an issue for SoOp systems. As seen in Figures 1.2-1.4, only a few bands are specifically allocated for scientific Earth observation, with most being above 1 GHz. Many others that could possibly be used are shared between federal and non-federal entities [24].


Figure 1.2.: FCC Spectrum Allocation Legend [24]

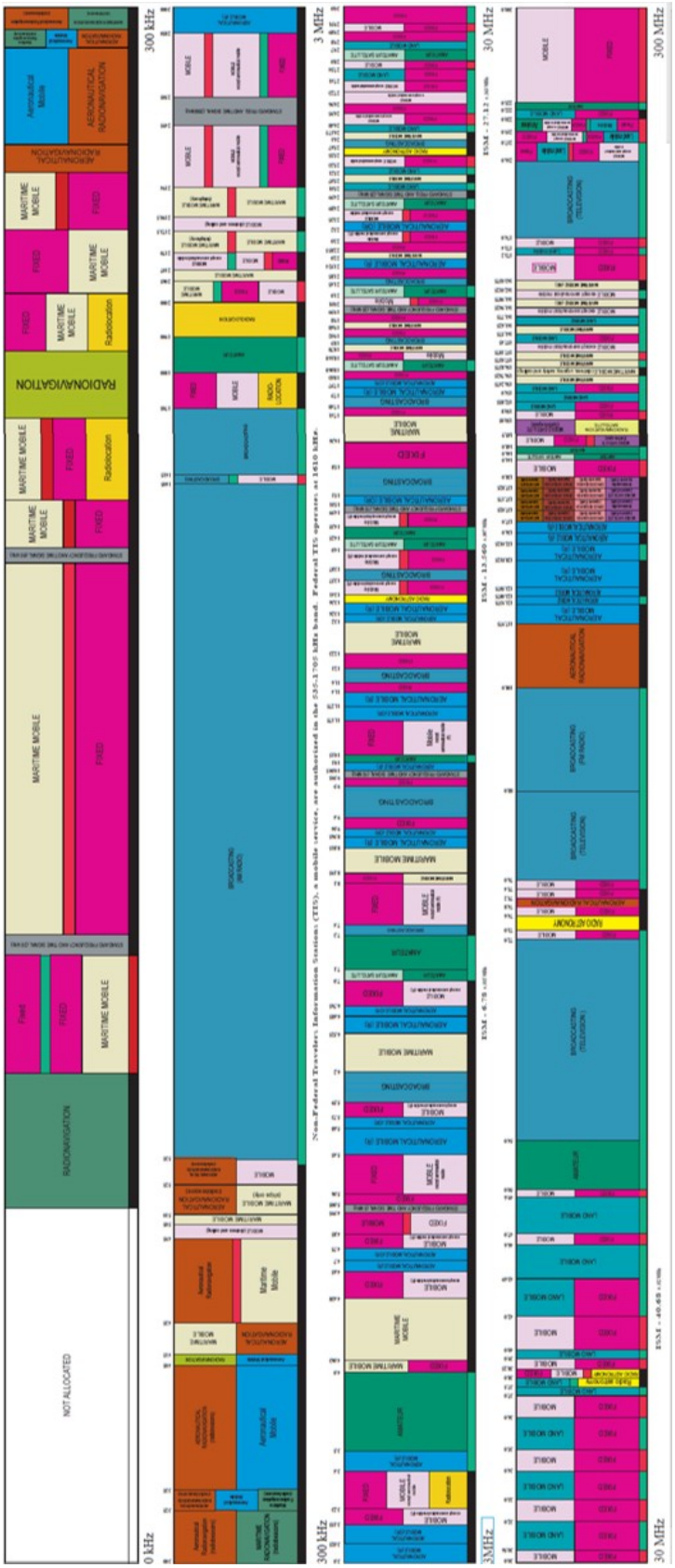


Figure 1.3.: FCC Spectrum Allocation by Frequency, 0-300 MHz [24]

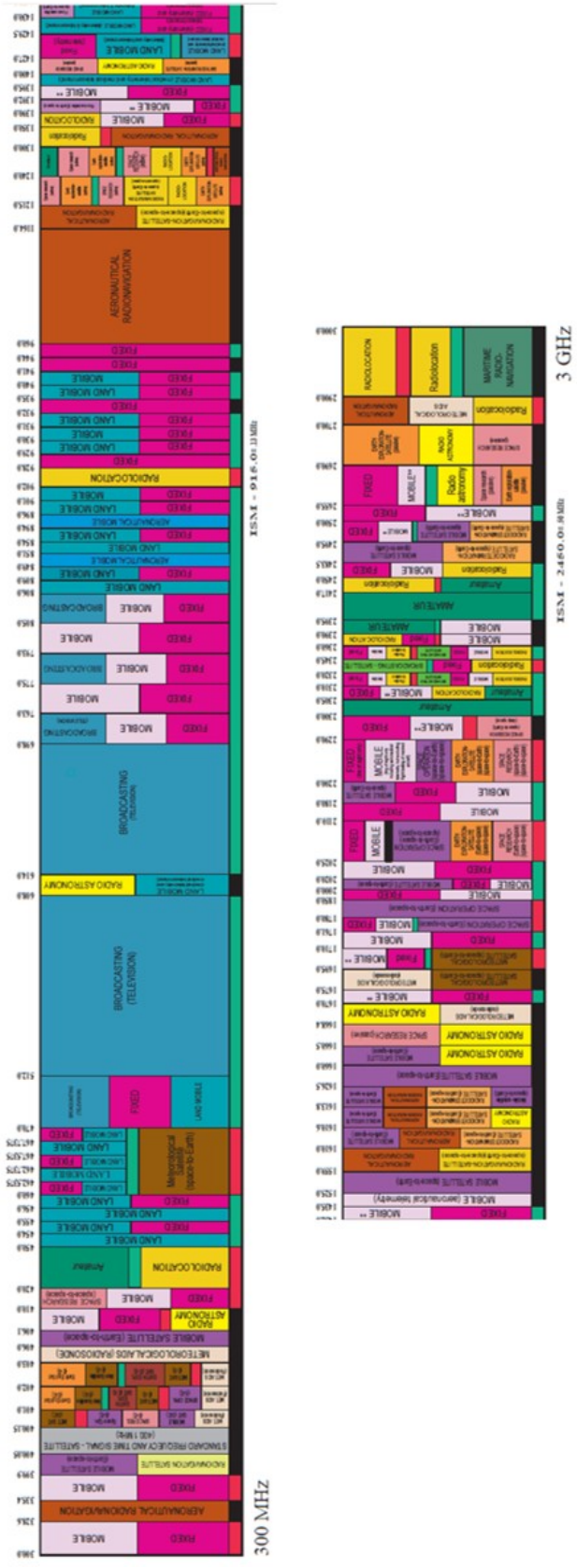


Figure 1.4.: FCC Spectrum Allocation by Frequency, 300 MHz-3 GHz [24]

Competition amongst this already packed signal spectrum is rendered moot for SoOp as it can utilize a wider range of frequencies in bands of the spectrum not typically allocated for scientific use. Another advantage is that transmitters like DirecTV, ORBCOMM, SiriusXM, etc. usually have a large signal power and the SoOp configuration places the receiver on the forward scatter of this signal. This allows for greater signal-to-noise ratio with smaller antennas than normal remote sensing systems. SoOp also only needs a receiver, which allows for a smaller instrument/satellite that requires less power than one made of both an active transmitter and receiver. Lastly, different frequencies, especially P-band, are able to penetrate further into the ground than others; the L-band GNSS used by systems such as CYGNSS or SMAP is only able to penetrate the first few centimeters of soil.

While P-band (225-390 MHz) currently represents the focus of many SoOp studies, using frequencies even lower than 225 MHz can offer even better performance. P-band instruments can reach about 25 centimeters below the soil, for certain soil types, whereas I-Band signals in the 135 MHz range can penetrate down to approximately 40 centimeters beneath the surface. This represents a 60% increase in penetration depth of the root zone. Having a longer wavelength will also enable better vegetation penetration and allow for signal coherence on surfaces with a larger average surface roughness than if P-band was used.

The work in this thesis focuses on the development of an I-Band Signals of Opportunity system using ORBCOMM at 137-138 MHz. An instrument was designed and constructed for mounting to an Unmanned Aerial Vehicle (UAV) for the remote sensing of root zone soil moisture (RZSM). This instrument was designed with calibration capabilities to allow for better estimation of soil moisture. Other system components such as power, instrument control, data recording, and ground support code were also developed. Specular point mapping software was created to assist with mission planning. A compact, deep-penetrating, mobile remote sensing system, such as the one designed in this thesis, would be of valuable use in fields such as precision agriculture and forestry.

# 2. THEORETICAL DERIVATIONS

Signals of Opportunity (SoOp) is a reflectometry-based remote sensing method which employs a receiver in a bi-static configuration. In this type of configuration, the transmitter and receiver of a signal are in different locations; unlike a traditional bi-static system, however, a SoOp instrument only comprises the receiver portion of the system. The transmissions used for remote sensing in this method are provided by already existing digital communications.

## 2.1 Properties of Electromagnetic Waves

Electromagnetic waves are fields of electromagnetic energy propagating through a medium. They are composed of both electric and magnetic fields. As such, EM waves can be modeled as a function of both time and position. A basic representation of this, assuming a wave oriented in the $\hat{x}$ direction with propagation in the $\hat{z}$ direction would be:

$$E = \hat{x}E_x(z,t) \tag{2.1}$$

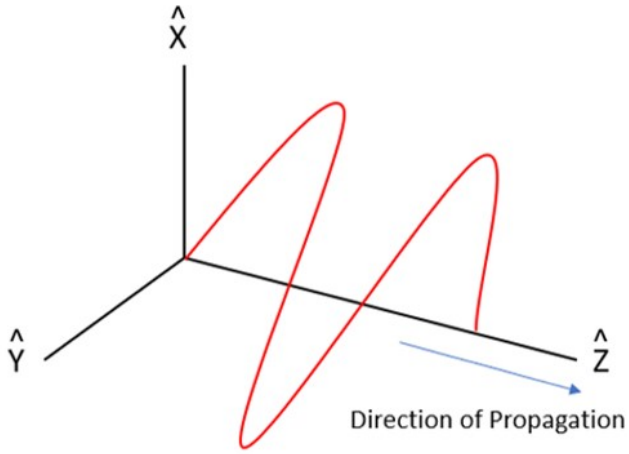


Figure 2.1.: Diagram of Wave Propagation

When waves interact with one another, the parts that are coherent with each other will result in constructive and destructive interference depending on the alignment of the two waves. The overall result of these interferences is known as an interference pattern.

### 2.1.1 Wave Polarization

The geometry of oscillation of an electromagnetic wave is referred to as wave polarization. Electromagnetic waves can be linearly polarized, elliptically polarized, or circularly polarized, which is itself a special case of elliptically polarized. Circular polarization is further divided into Left Hand Circular Polarization (LHCP) and Right Hand Circular Polarization (RHCP) based upon the direction of "rotation" with respect to the direction of travel. Wave polarization can be expressed mathematically as:

$$E = \hat{x}E_x(z,t) + \hat{y}E_y(z,t) \tag{2.2}$$

where

$$E_x(z,t) = E_1\cos(\omega t - \beta z) \tag{2.3}$$

$$E_y(z,t) = E_2\cos(\omega t - \beta z + \alpha) \tag{2.4}$$

If $\alpha$ is $\frac{\pi}{2}$, the wave is LHCP. If $\alpha$ is $-\frac{\pi}{2}$, the wave is RHCP. A wave with one component equaling zero is linearly polarized in the direction of the other component.

When a wave passes through the ionosphere, interactions with free electrons will cause the polarization of the wave to change, a process known as Faraday rotation or the Faraday effect. Linearly polarized waves become elliptical and elliptically polarized waves are rotated about the axis of propagation. Because antennas typically can only send and receive signals with one specific polarization, the Faraday effect presents both challenges and opportunities for exploitation by satellite communication engineers. Satellites commonly transmit on RHCP or LHCP to avoid this effect altogether.

### 2.1.2 Specular Reflection

The reflection of a wave is considered to be specular if a single wave hits a smooth, semi-infinite medium in a single spot and is reflected at the same angle as the incident angle that the wave came in at. This is exactly the same as to what is usually meant by the word "reflection" in general: a single wave reflecting off of a singular point like a mirror.

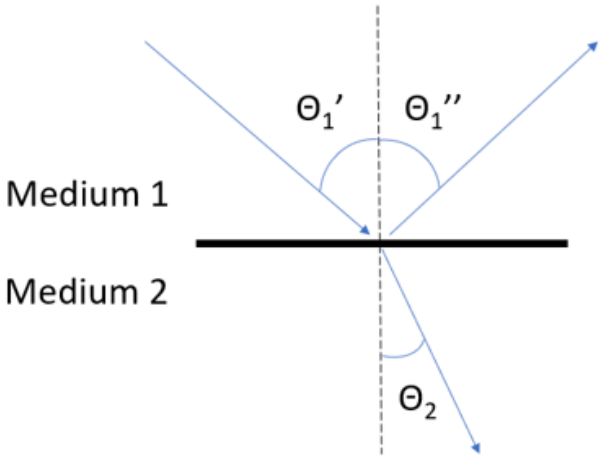


Figure 2.2.: Reflection and Refraction of EM Wave

As shown in Figure 2.2, a wave reflection is considered specular when $\theta_1'$, the angle of incidence, is equal to $\theta_1''$, the angle of reflection. If they are not equal and the wave is reflected in different or multiple directions, the reflection is said to be diffuse.

The Rayleigh criterion for resolution defines the distance between two sources at which both can be distinctly resolved from one another. An extension of this for surface roughness is that a surface may be considered smooth if the phase difference between an incident and reflected wave is less than $\frac{\pi}{2}$ radians. The Rayleigh criterion in this case is written as:

$$\frac{\lambda}{8\cos\theta} \tag{2.5}$$

where $\lambda$ is the wavelength and $\theta$ is incidence angle of the wave. As long as the RMS surface height of the reflection point above the "flat" surface or zero surface height, $\sigma_z$, is less than or equal to the Rayleigh criterion:

$$\sigma_z \leq \frac{\lambda}{8\cos\theta} \tag{2.6}$$

the surface may be considered smooth and thus reflections are specular. For I-Band frequencies with a wavelength of approximately 2.18 meters, the Rayleigh criterion ranges between 27.25 centimeters for a zero degree incidence angle and 156.93 centimeters for an 80 degree incidence angle.

### 2.1.3 Fresnel Zones

In wireless communications, obstructions in the line-of-sight between two points can cause issues with the proper functioning of the system. Between two points, the Fresnel zone is used to define the elliptical area where such interference can occur. Along a single transmission path there are normally multiple Fresnel zone ellipsoids. This same principle, while usually referring to an above-the-ground area between a transmitter and receiver, can also be applied to remote sensing on a surface. In

remote sensing, the size of a Fresnel zone directly impacts the size of the reflection zone, which in turn contains the specular point of reflection.

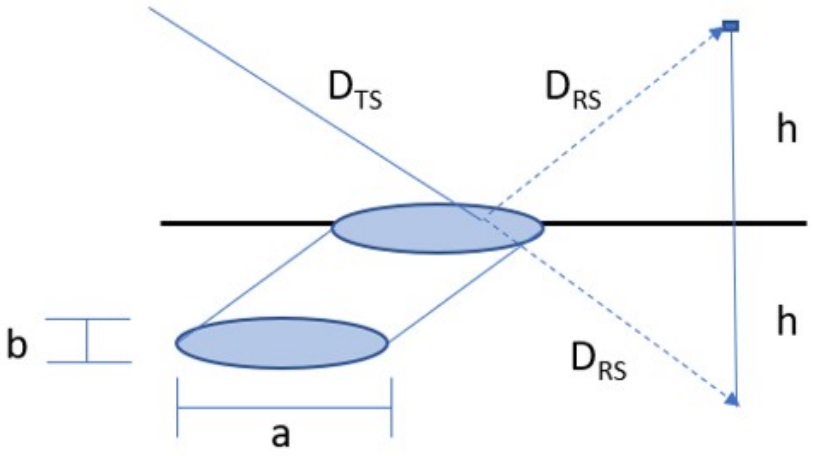


Figure 2.3.: Fresnel Zone Diagram

The size of a Fresnel zone is defined as an ellipsoid with semi-minor axis:

$$b = \sqrt{n\lambda \frac{D_{TS} D_{RS}}{D_{TS} + D_{RS}}} \tag{2.7}$$

where $n$ represents the Fresnel zone number, $\lambda$ represents the signal wavelength, and $D$ represents the distance between the transmitter and specular point and the receiver and specular point. The semi-minor axis can also be approximated using the height, $h$, and elevation of the transmitter, $\theta$:

$$b = \sqrt{\frac{\lambda h}{\sin\theta}} \tag{2.8}$$

The semi-major axis can then be defined as:

$$a = \frac{b}{\sin\theta} \tag{2.9}$$

### 2.1.4 Interactions with Media

#### Wave Properties and Reflectance

The surfaces typically involved in remote sensing are those such as water or soil, which are a combination of multiple media. When an electromagnetic wave strikes and passes through two or more different media, waves can either reflect or refract, also known as transmission. As it passes between media, the wave can split and partially reflect and partially refract depending on the medium. This can be seen in Figure 2.2, where the wave can refract at an angle of $\theta_2$ as it passes into a second medium.

Fresnel coefficients are used to define the ratio between the electric field amplitude of the reflected or refracted wave and that of the incident wave. These ratios are due to the differences in dielectric constant between the media. The Fresnel reflection coefficient for a horizontally-polarized wave, based upon incidence angle $\theta$ and complex dielectric constants $\varepsilon$, is the ratio of the electric fields between the first and second medium:

$$\rho_h = \frac{E''_{H1}}{E'_{H1}} = \frac{\cos(\theta_1) - \sqrt{\varepsilon_{2r} - \sin^2(\theta_1)}}{\cos(\theta_1) + \sqrt{\varepsilon_{1r} - \sin^2(\theta_1)}} \tag{2.10}$$

For vertically polarized wave, the Fresnel reflection coefficient is:

$$\rho_v = \frac{E''_{V1}}{E'_{V1}} = \frac{\varepsilon_{2r}\cos(\theta_1) - \sqrt{\varepsilon_{2r} - \sin^2(\theta_1)}}{\varepsilon_{2r}\cos(\theta_1) + \sqrt{\varepsilon_{1r} - \sin^2(\theta_1)}} \tag{2.11}$$

To convert from horizontally and vertically polarized waves to circularly polarized waves, components are transformed according to the equation below. It is important to note that upon reflection, the polarization of a RHCP or LHCP wave may switch direction of rotation or become a summation of RHCP and LHCP signals.

$$\begin{bmatrix} \rho_{rr} & \rho_{rl} \\ \rho_{lr} & \rho_{ll} \end{bmatrix} = \frac{1}{2} \begin{bmatrix} \rho_h + \rho_v & \rho_h - \rho_v \\ \rho_h - \rho_v & \rho_h + \rho_v \end{bmatrix} \tag{2.12}$$

In the above equation, the first letter of the superscript denotes the circular polarization before reflection and the second letter denotes the polarization afterwards.

### Reflectivity

The aspect of a reflected wave that is often useful for remote sensing, and in Signals of Opportunity more specifically, is what is known as reflectivity. Reflectivity, denoted as $\Gamma$, can be approximated as the square of the magnitude of the Fresnel reflection coefficients:

$$\Gamma = |\rho^2| \tag{2.13}$$

Reflectivity is defined here as the ratio of signal power that is reflected from a surface to the direct signal power:

$$\Gamma = \frac{C_R}{C_D} \tag{2.14}$$

If it is assumed that the transmitter is at infinity and the altitude of the receiver is small, then the incident power at the antenna and the ground would be essentially the same. This, in turn, would make the estimated reflectivity equal to the true reflectivity.

### Penetration Depth in Soil

The penetration depth of an electromagnetic wave depends on its wavelength. The two share a directly proportional relationship; as wavelength increases (and frequency decreases), the penetration depth of the wave increases. Media composition and soil moisture content itself also plays a role in the penetration depth. Typically, wetter soils will have much less penetration depth than drier soils because of the increase in dielectric constant in wetter soils. The imaginary part of the dielectric constant relates to the energy loss of a penetrating wave so as the soil moisture and dielectric

constant increases, the penetration depth overall decreases. Penetration depth in soil can be modeled by:

$$PDepth = \frac{\lambda}{4\pi\sqrt{\epsilon''}} \tag{2.15}$$

where $\lambda$ represents the signal wavelength and $\epsilon''$ represents the imaginary part of the dielectric constant [14]. The effect of soil moisture and composition on the imaginary dielectric constant can be better seen by breaking down the imaginary dielectric constant as

$$\epsilon'' = [m_v^{\beta''} \epsilon_{fw}^{''\alpha}]^{1/\alpha} \tag{2.16}$$

where $m_v$ represents the volumetric soil moisture, $\epsilon''_{fw}$ represents the imaginary dielectric constant of water, $\alpha$ represents an empirical constant, and $\beta''$ represents the soil composition as a function of the percentages of clay and sand [25]:

$$\beta'' = 1.33797 - 0.603S - 0.166C \tag{2.17}$$

Figure 2.4 shows the penetration depth of various instruments at different wavelengths. These wavelengths, in numerical order, are I-Band, P-Band, L-Band, and S-Band. The I-Band signal used is ORBCOMM, P-Band is MUOS, L-Band is GPS, and S-Band is SiriusXM.

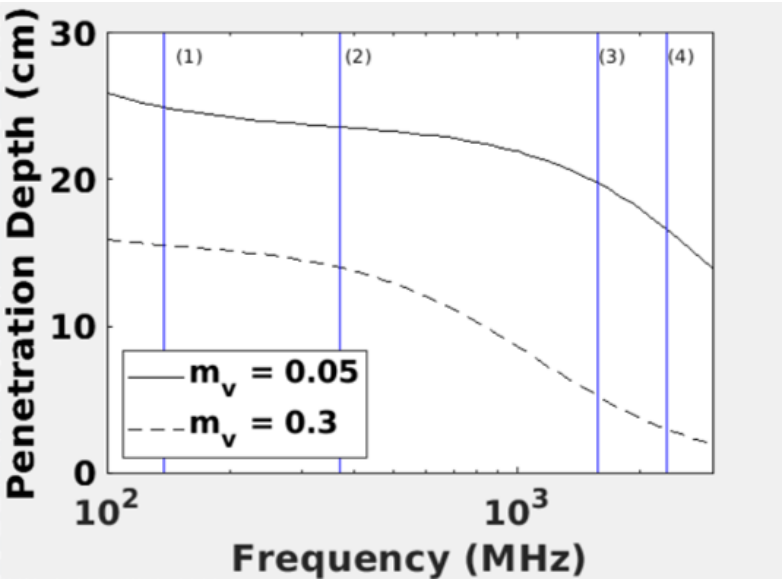


Figure 2.4.: Penetration Depth vs. Frequency

The model used to create Figure 2.4 estimates penetration depth by finding the dielectric constants for a layer of soil based on given soil moisture content, soil composition, and frequency. The dielectric constants are then used to calculate penetration depth and reflectivity. The model assumed loam soil with a standard composition of 40% silt, 40% sand, and 20% clay [25]. The model used volumetric soil constants ranging from 0.05 as a low to 0.50 as a high. The medium value was 0.20. Constants at 0.05 and 0.30 are plotted here for convenience.

## 2.2 Signals of Opportunity Model

A Signals of Opportunity system focuses on the design of the receiver portion of a bi-static system. This system is designed using the ORBCOMM constellation as the transmitter. The receiver collects two signals: one direct and one reflected from the ground. Reflectivity can be estimated from the ratio of the powers of the reflected and direct signals.

### 2.2.1 Signal Ray Path

Figure 2.5 demonstrates the ray path for an ideal UAV-based Signal of Opportunity instrument. The instrument carries both a skyward facing antenna and an Earth facing antenna.

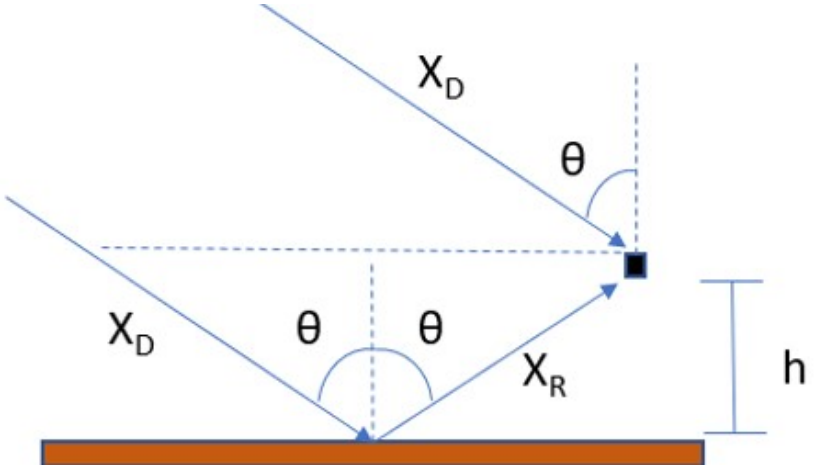


Figure 2.5.: Signals of Opportunity Ray Path Model

The following assumptions are used:

1. All signal reflections are specular.
    - In accordance with Equation 2.6, this assumption is valid as long as the RMS of the surface height standard deviation of the test site does not vary by more than 27.25 centimeters.
2. There is not perfect isolation between the sky and earth antennas.
    - The gain patterns of the antennas used will result in the antennas seeing both some portion of the direct and reflected signals.

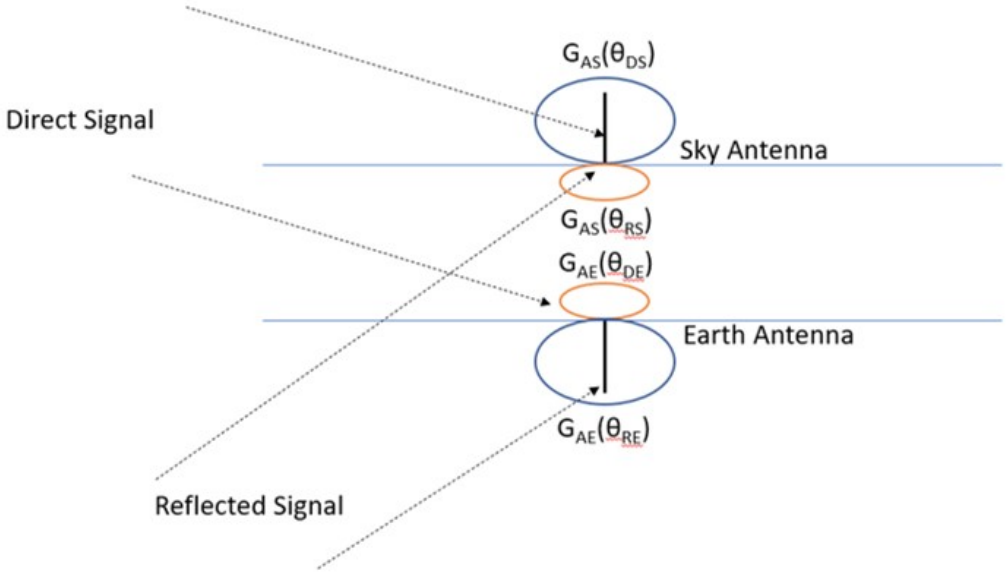


Figure 2.6.: Non-Isolation Ray Path Model

3. The distance between the receiver and transmitter is infinite.

    - The angle of incidence and signal power at the direct antenna and the specular reflection point can be assumed as the same.

The transmitted signals are comprised of the their power $C$, modulation $s(t)$, and frequency of the carrier $\omega_c$.

$$X_T = \sqrt{C}s(t)e^{j\omega_c t} \tag{2.18}$$

At the antennas, the direct and reflected signals will contain a carrier phase shift $\phi$, time delay from transmission to reception $\tau$, and Doppler shift $\omega_{Dop}$. The reflected signal contains reflectivity, $\Gamma$. The direct and reflected signals are modeled as:

$$X_D(t) = \sqrt{C_D}s(t-\tau_D)e^{j((\omega_c+\omega_{Dop})t+\phi_D)} \tag{2.19}$$

$$X_R(t) = \sqrt{C_D\Gamma}s(t-\tau_R)e^{j((\omega_c+\omega_{Dop})t+\phi_R)} \tag{2.20}$$

Each antenna will receive both the direct and reflected signal due to their non-isolated nature.

Because it is assumed that the distance between the transmitter and receiver is infinite, the ray paths of the direct and reflected signal are parallel to one another. As such, the distance between the lengths of the direct and reflected signal paths is related to the time difference between the delays of the direct and reflected signal paths:

$$d = c(\tau_R - \tau_D) = 2h\cos(\theta) \tag{2.21}$$

where $\theta$ represents the angle of incidence, $h$ is the receiver height, and $c$ is the speed of light.

### 2.2.2 Correlation Operator

The essential operation of a SoOp receiver is to perform the time-domain correlation between two received signals. For our purposes, this is defined as the integrated product of one signal with the complex conjugate of the other signal offset at some time delay $\tau$:

$$R_{12}(\tau) = \frac{1}{T_I}\int_{T_I} x_1(t)x_2^*(t-\tau)dt = \langle x_1(t)x_2^*(t-\tau)\rangle \tag{2.22}$$

The time-domain autocorrelation of a signal is the correlation of a signal with itself.

$$R_{11}(\tau) = \frac{1}{T_I}\int_{T_I} x_1(t)x_1^*(t-\tau)dt = \langle x_1(t)x_1^*(t-\tau)\rangle \tag{2.23}$$

The average power of the signal is approximated using the Ergodic hypothesis as:

$$P \approx \frac{1}{T_I}R_{11}(0) \tag{2.24}$$

### 2.2.3 Noise Model

This system considers only thermal noise from the antennas and front-end RF equipment. It is assumed all noise in this system, $\eta(t)$, is additive white Gaussian

with an applied filter that limits the noise bandwidth to $B$. The power spectral density of this noise would be $N_0$ for noise frequencies inside the bandwidth and zero for all else. The total noise power is modeled here as the equivalent thermal noise power:

$$P_\eta = N_0 B = kTB \tag{2.25}$$

where $k$ represents the Boltzmann's constant, $T$ the applicable noise temperature, and $B$ the noise bandwidth. The noise is zero mean with expected values:

$$E\{\eta(t)\} = 0 \tag{2.26}$$

$$E\{\eta(t)\eta(t+\tau)\} = R_\eta(t) \tag{2.27}$$

Approximating $\eta(t)$ as the output of an ideal bandpass filter with frequency response:

$$H(f) = \begin{cases} 1, |f| \leq \frac{B}{2} \\ 0, |f| > B \end{cases} \tag{2.28}$$

then the noise power correlation at time delay $\tau$ is:

$$R_\eta(\tau) = kT \int_{-\infty}^{\infty} H(f) e^{2\pi f \tau j} df = \int_{-B/2}^{B/2} e^{2\pi f \tau j} df = kTBsinc(B\tau) \tag{2.29}$$

where $T$ is the sum of all equivalent noise temperatures in the signals being correlated.

The noise sources in RF front end are composed of two identical hardware systems ($\eta_1$ and $\eta_2$) and a noise injection diode ($\eta_{Dio}$). Noise will also be present from the antennas. Only noise from the same source correlated with itself with have a non-zero correlation and will become a sum of the noise temperatures:

$$E\{\eta_1, \eta_2^*\} = E\{\eta_1, \eta_{Dio}^*\} = E\{\eta_2, \eta_{Dio}^*\} = 0 \tag{2.30}$$

$$R_{\eta_1}(\tau) = k(T_1 + T_{AS} + T_{Dio})Bsinc(B\tau) \tag{2.31}$$

$$R_{\eta_2}(\tau) = k(T_2 + T_{AE} + T_{Dio})Bsinc(B\tau) \tag{2.32}$$

$$R_{\eta_1,\eta_2}(\tau) = kT_{Dio}Bsinc(B\tau) \tag{2.33}$$

### 2.2.4 Signal Model

The instrument is composed of two channels, channel 1 and channel 2. The signals received at the antennas are filtered and amplified by the RF front end before being down-converted and converted from analog to digital at the USRP Software Defined Radio. Each channel will contain a combination of the direct and reflected signals, along with noise from the RF systems and antennas.

$$X_1(t) = \sqrt{G_1}\big[\sqrt{G_{AS}(\theta_{DS})}X_D(t)+\sqrt{G_{AS}(\theta_{RS})}X_R(t)+\eta_1(t)+\eta_{AS}(t)+\eta_{Dio}(t)\big]e^{-j(\omega_I+\omega_c)t} \tag{2.34}$$

$$X_2(t) = \sqrt{G_2}\big[\sqrt{G_{AE}(\theta_{DE})}X_D(t)+\sqrt{G_{AE}(\theta_{RE})}X_R(t)+\eta_2(t)+\eta_{AE}(t)+\eta_{Dio}(t)\big]e^{-j(\omega_I+\omega_c)t} \tag{2.35}$$

Combining the signal components for each antenna and the noise sources for each channel simplifies the equations to :

$$X_1(t) = \sqrt{G_1}\big[X_{S1}(t) + \eta_{S1}(t)\big]e^{-j(\omega_I+\omega_c)t} \tag{2.36}$$

$$X_2(t) = \sqrt{G_2}\big[X_{S2}(t) + \eta_{S2}(t)\big]e^{-j(\omega_I+\omega_c)t} \tag{2.37}$$

The reflectivity measurement, $\Gamma$, is contained in $X_{S1}(t)$ and $X_{S2}(t)$ along with the antenna gain patterns that are either provided by the manufacturer or calibrated. Obtaining the reflectivity measurement is compounded by the unknowns present in the system from the hardware gain, $G_1$, and $G_2$, and the noise from the systems and antennas. Because the noise is modeled as thermal, the unknowns from the noise are the noise temperatures of the antennas and components: $T_{AE}$, $T_{AS}$, $T_1$, and $T_2$. The noise temperature of the noise diode is a constant, known value. To enable finding reflectivity, the instrument must be calibrated to find these unknown values. Example

methods for finding reflectivity are discussed in Appendix B and are independent from the calibration.

The signals from channel 1 and 2 are auto and cross-correlated to setup calibration. The autocorrelation of one channel with itself is defined as:

$$R_{11}(\tau) = \langle X_1(t)X_1^*(t+\tau)\rangle = G_1\big[\langle X_{S1}(t)X_{S1}^*(t+\tau)\rangle + \langle \eta_{S1}(t)X_{S1}^*(t+\tau)\rangle + \langle X_{S1}(t)\eta^*(t+\tau)\rangle + \langle \eta_{S1}(t)\eta_{S1}^*(t+\tau)\rangle\big]e^{j(\omega_I+\omega_c)\tau} \quad (2.38)$$

This will be a random variable with mean:

$$E\{R_{11}(\tau)\} = G_1\big[E\{\langle X_{S1}(t)X_{S1}^*(t+\tau)\rangle\} + E\{\langle \eta_{S1}(t)\eta_{S1}(t+\tau)\rangle\}\big]e^{j(\omega_I+\omega_c)\tau} \quad (2.39)$$

Applying the Ergodic hypothesis to a correlation with long enough integration time to approach the ensemble average, it is assumed that:

$$E\{\langle X_{S1}(t)X_{S1}^*(t+\tau)\rangle\} = R_{S_{11}}(\tau) \quad (2.40)$$

Combining this with the results of Equation 2.29, the auto and cross-correlations of the signals at channels 1 and 2 are:

$$R_{11}(\tau) = G_1\big[R_{S_{11}}(\tau) + k(T_1 + T_{AS} + T_{Dio})Bsinc(B\tau)\big]e^{j(\omega_I+\omega_c)\tau} + \epsilon_{11} \quad (2.41)$$

$$R_{22}(\tau) = G_2\big[R_{S_{22}}(\tau) + k(T_2 + T_{AE} + T_{Dio})Bsinc(B\tau)\big]e^{j(\omega_I+\omega_c)\tau} + \epsilon_{22} \quad (2.42)$$

$$R_{12}(\tau) = \sqrt{G_1G_2}\big[R_{S_{12}}(\tau) + kT_{Dio}Bsinc(B\tau)\big]e^{j(\omega_I+\omega_c)\tau} + \epsilon_{12} \quad (2.43)$$

The errors, $\epsilon$, in the correlations are assumed to be zero mean and represent the system noise after averaging.

$$\epsilon_{11} = R_{11}(\tau) - E\{R_{11}(\tau)\} \quad (2.44)$$

$$\epsilon_{22} = R_{22}(\tau) - E\{R_{22}(\tau)\} \quad (2.45)$$

$$\epsilon_{12} = R_{12}(\tau) - E\{R_{12}(\tau)\} \tag{2.46}$$

## 2.3 Calibration States

The purpose of calibration is to solve for unknown system properties, such as gains and noise temperatures, to allow for the estimation of reflectivity. The calibration method will remain the same regardless of the reflectivity retrieval algorithm used. The microwave front-end attached to the UAV is designed with three main states: through, cold noise, and reference load. All of the calibration states can have noise injected into the system from a controllable noise-injection diode with a known noise temperature. This gives a total of six distinct possible states. The front-end is composed of two identically designed RF systems.

### 2.3.1 Through State

The through state is the state in which direct and reflected signals are collected. Figure 2.7 traces this path through the front-end diagram, with green representing the through state itself and red representing the optional noise injection.

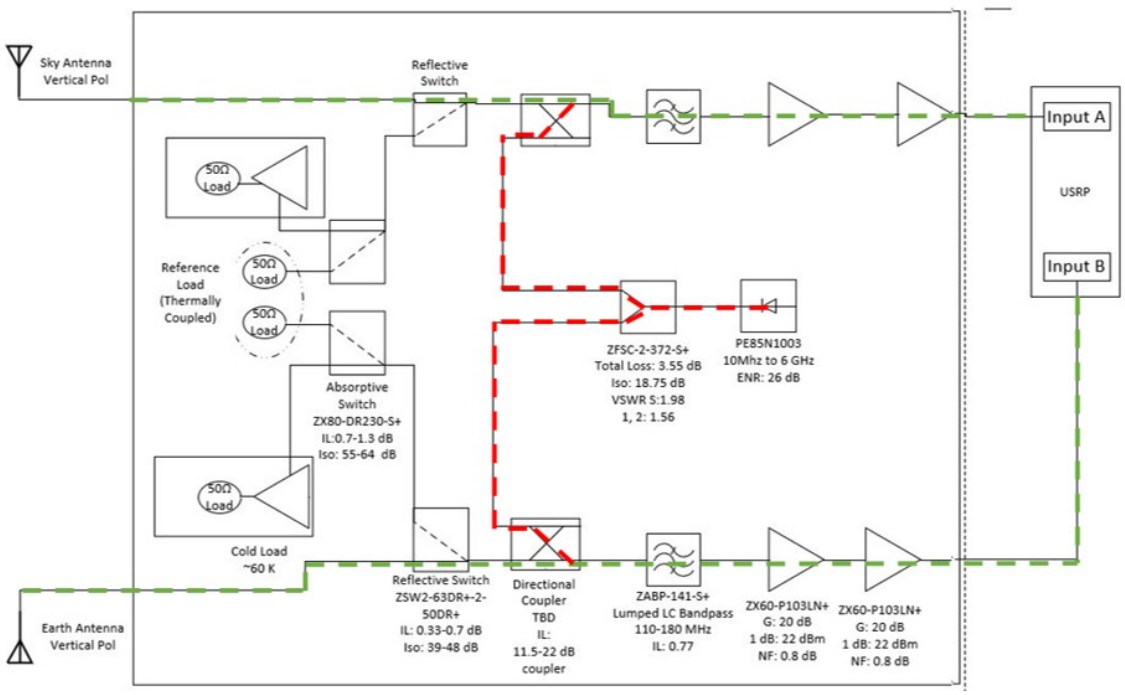


Figure 2.7.: Through State

The signals and correlations for this state are those already modeled in section 2.2.4.

$$X_1(t) = \sqrt{G_1}\big[X_{S1}(t) + \eta_{S1}(t)\big]e^{-j(\omega_I+\omega_c)t} \tag{2.47}$$

$$X_2(t) = \sqrt{G_2}\big[X_{S2}(t) + \eta_{S2}(t)\big]e^{-j(\omega_I+\omega_c)t} \tag{2.48}$$

$$R_{11_T}(\tau) = G_1\big[R_{S_{11}}(\tau) + k(T_1 + T_{AS} + T_{Dio})Bsinc(B\tau)\big]e^{j(\omega_I+\omega_c)\tau} \tag{2.49}$$

$$R_{22_T}(\tau) = G_2\big[R_{S_{22}}(\tau) + k(T_2 + T_{AE} + T_{Dio})Bsinc(B\tau)\big]e^{j(\omega_I+\omega_c)\tau} \tag{2.50}$$

$$R_{12_T}(\tau) = \sqrt{G_1G_2}\big[R_{S_{12}}(\tau) + kT_{Dio}Bsinc(B\tau)\big]e^{j(\omega_I+\omega_c)\tau} \tag{2.51}$$

In order to solve for reflectivity contained in $R_{11_T}(\tau)$,$R_{22_T}(\tau)$, and $R_{12_T}(\tau)$, the system gains and noise temperatures, and antenna gains must be estimated. This is accomplished through the information provided by the other calibration states. The full method for calibration is shown later in 2.3.4.

### 2.3.2 Active Cold Load State

The active cold load state is an active noise state where no signal from an antenna is input into channel 1 or channel 2. Rather, these inputs are made up of the noise of an active "cold" noise load whose physical temperature is measured. The noise diode can either be turned on or off in any case but is included for reference. Figure 2.8 traces the cold load state path through the front-end diagram in green, with red again representing the optional noise injection.

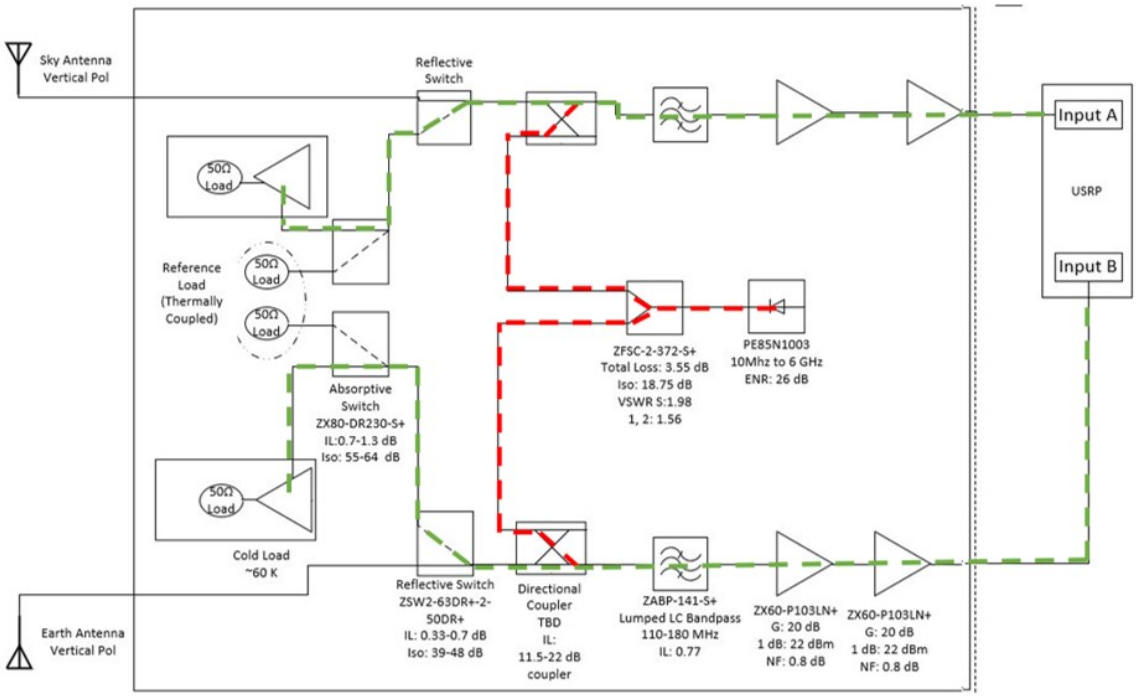


Figure 2.8.: Active Cold Load State

The signals received at the USRP are:

$$X_1(t) = \sqrt{G_1}(\eta_1 + \eta_{Cold_1} + \eta_{Dio})e^{j(\omega_I+\omega_c)t} \tag{2.52}$$

$$X_2(t) = \sqrt{G_2}(\eta_2 + \eta_{Cold_2} + \eta_{Dio})e^{j(\omega_I+\omega_c)t} \tag{2.53}$$

Correlating the two channels:

$$R_{11c}(\tau) = G_1 kBsinc(B\tau)(T_1 + T_{Cold_1} + T_{Dio})e^{j(\omega_I+\omega_c)\tau} \tag{2.54}$$

$$R_{22c}(\tau) = G_2 kBsinc(B\tau)(T_2 + T_{Cold_2} + T_{Dio})e^{j(\omega_I+\omega_c)\tau} \tag{2.55}$$

$$R_{12c}(\tau) = \sqrt{G_1 G_2} kBT_{Dio}sinc(B\tau)e^{j(\omega_I+\omega_c)\tau} \tag{2.56}$$

Expanded correlations are provided in Appendix B.

Reflectivity is not present, as no signals are received from the antennas. However, this state provides more equations for solving for the various system unknowns. Specifically, the system gains $G$ and noise temperatures $T$ are unknown is this state. The cold load noise temperatures $T_{Cold}$ are estimated through measuring the physical temperature of the device.

### 2.3.3 Reference Load State

The reference load state is similar in fashion to the cold noise state. The signals received by the antennas are not received by USRP and only noise from the reference loads is inputted into the system. The reference loads are comprised of two thermally coupled 50 ohm terminators. In the same manner as the active cold load, the system noise temperatures of the reference loads are known. Figure 2.9 traces the reference load state through the front-end diagram in green, with red again representing the optional noise injection.

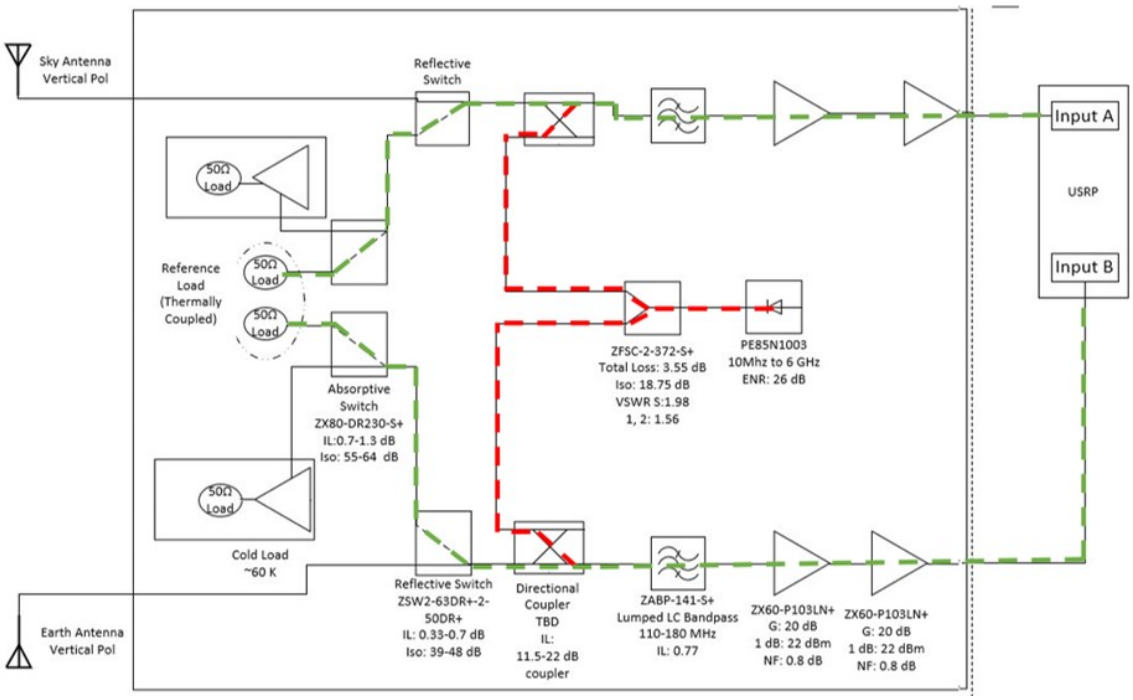


Figure 2.9.: Reference Load State

The signals received at the USRP are:

$$X_1(t) = \sqrt{G_1}(\eta_1 + \eta_{Ref_1} + \eta_{Dio})e^{j(\omega_I+\omega_c)t} \tag{2.57}$$

$$X_2(t) = \sqrt{G_2}(\eta_2 + \eta_{Ref_2} + \eta_{Dio})e^{j(\omega_I+\omega_c)t} \tag{2.58}$$

Correlating the two channels:

$$R_{11r}(\tau) = G_1 kBsinc(B\tau)(T_1 + T_{Ref_1} + T_{Dio})e^{j(\omega_I+\omega_c)\tau} \tag{2.59}$$

$$R_{22r}(\tau) = G_2 kBsinc(B\tau)(T_2 + T_{Ref_2} + T_{Dio})e^{j(\omega_I+\omega_c)\tau} \tag{2.60}$$

$$R_{12r}(\tau) = \sqrt{G_1 G_2} kBT_{Dio}sinc(B\tau)e^{j(\omega_I+\omega_c)\tau} \tag{2.61}$$

This state is similar to the cold load state where the unknowns are the system gains and noise temperatures. The reference load temperatures will also be estimated from measuring the physical temperature of the reference loads.

### 2.3.4 Solving for Unknown System Parameters

The auto and cross-correlations for each calibration state form a system of equations with various knowns and unknowns. These equations are used to obtain estimates of the unknown system gains and noise temperatures. An algorithm for doing so is:

Step 1: Reorganize $R_{11c}$ (Equation 2.54) for $G_1$ at $\tau = 0$

$$G_1 = \frac{R_{11c}(0)}{kB(T_1 + T_{Cold_1} + T_{Dio})} \tag{2.62}$$

Likewise

$$G_2 = \frac{R_{22c}(0)}{kB(T_2 + T_{Cold_2} + T_{Dio})} \tag{2.63}$$

Step 2: Substitute Equation 2.62 into Equation 2.59

$$R_{11r}(0) = \frac{R_{11c}(0)}{kB(T_1 + T_{Cold_1} + T_{Dio})} kB(T_1 + T_{Ref_1} + T_{Dio}) \tag{2.64}$$

Rearranging for $T_1$ gives:

$$T_1 = \frac{R_{11c}(0)(T_{Ref_1} + T_{Dio}) - R_{11r}(0)(T_{Cold1} + T_{Dio})}{R_{11r}(0) - R_{11c}(0)} \tag{2.65}$$

Following the same procedure using Equations 2.63 and 2.60:

$$T_2 = \frac{R_{22c}(0)(T_{Ref_2} + T_{Dio}) - R_{22r}(0)(T_{Cold2} + T_{Dio})}{R_{22r}(0) - R_{22c}(0)} \tag{2.66}$$

Once $T_1$ and $T_2$ are known, these are inserted into Equations 2.62 and 2.63, allowing $G_1$ and $G_2$ to be estimated.

### 2.3.5 Antenna Gain Parameters

Antenna gain patterns can be simulated or estimated from the instrument. $T_1$ is found from Equation 2.65. $T_{AS}$ is estimated through the following integral:

$$T_{AS} = \frac{\int_0^{2\pi}\int_0^{\pi} T_B(\theta,\phi)D(\theta,\phi)\sin(\theta)d\theta d\phi}{\int_0^{2\pi}\int_0^{\pi} D(\theta,\phi)\sin(\theta)d\theta d\phi} \tag{2.67}$$

where $T_B$ is the background noise temperature and $D$ is the antenna gain pattern.

### 2.3.6 Example Reflectivity Measurement

The following provides an example of solving for the reflectivity measurement to show how the correlations can be used in conjunction with the instrument calibration. Other retrieval algorithms are presented in Appendix B. This algorithm will assume perfect isolation to provide a simple example. In solving such as case, reflectivity can be found from evaluating the through state cross-correlation at $\tau_{RD}$ and one of the through state auto-correlations at $\tau = 0$. Doing so, the signals at the antennas will be:

$$X_{S1}(t) = \sqrt{G_{AS}}X_D(t) = \sqrt{G_{AS}C_D}s(t-\tau_D)e^{j(\omega_c+\omega_I)t+j\phi_D} \tag{2.68}$$

$$X_{S2}(t) = \sqrt{G_{AE}}X_R(t) = \sqrt{G_{AE}C_D\Gamma}s(t-\tau_R)e^{j(\omega_c+\omega_I)t+j\phi_R} \tag{2.69}$$

The signal component correlations needed to solve for reflectivity are:

$$R_{S11}(0) = \langle X_{S1}(t) X_{S1}^{*}(t) \rangle = G_{AS} C_D \tag{2.70}$$

$$R_{S12}(\tau_{RD}) = \sqrt{G_{AS} G_{AE} \Gamma} C_D e^{j(\omega_c + \omega_I)\tau_{RD} + j\phi_{RD}} \tag{2.71}$$

where

$$\tau_{RD} = \tau_R - \tau_D \tag{2.72}$$

$$\phi_{RD} = \phi_R - \phi_D \tag{2.73}$$

From the through state correlations,

$$R_{11_T}(0) = G_1 \big[ R_{S_{11}}(0) + k(T_1 + T_{AS} + T_{Dio}) B \big] e^{j(\omega_I + \omega_c)\tau} \tag{2.74}$$

$$R_{12_T}(\tau_{RD}) = \sqrt{G_1 G_2 G_{AS} G_{AS} \Gamma} C_D \tag{2.75}$$

$$\eta_{11} = k(T_1 + T_{AS} + T_{Dio}) B \tag{2.76}$$

By dividing the cross correlation by the autocorrelation with the noise floor subtracted out, one obtains an expression that can be rearranged for reflectivity.

$$\frac{R_{12_T}(\tau_{RD})}{R_{11_T}(0) - \eta_{11}} = \frac{\sqrt{G_1 G_2 G_{AS} G_{AE} \Gamma} C_D}{G_1 G_{AS} C_D} \tag{2.77}$$

Rearranging for reflectivity:

$$\Gamma = \left( \frac{R_{12_T}(\tau_{RD})}{R_{11_T}(0) - \eta_{11}} \right)^2 \frac{G_1 G_{AS}}{G_2 G_{AE}} \tag{2.78}$$

# 3. INSTRUMENT DESIGN

For this experiment, an instrument was designed and constructed to allow for the collection of I-band, or VHF satellite signals, specifically from the ORBCOMM communication constellation operating between 137 and 138 MHz. It is designed for mounting onto a hexacopter Unmanned Aerial Vehicle to allow for dynamic collection of these signals and their subsequent reflections. All power and RF related equipment is placed inside of a metal enclosure for mitigation of radio frequency interference (RFI). The system collects both a direct and reflected signal to be used for remote sensing using the Signals of Opportunity (SoOp) method. A diagram of the overall system design is shown below.

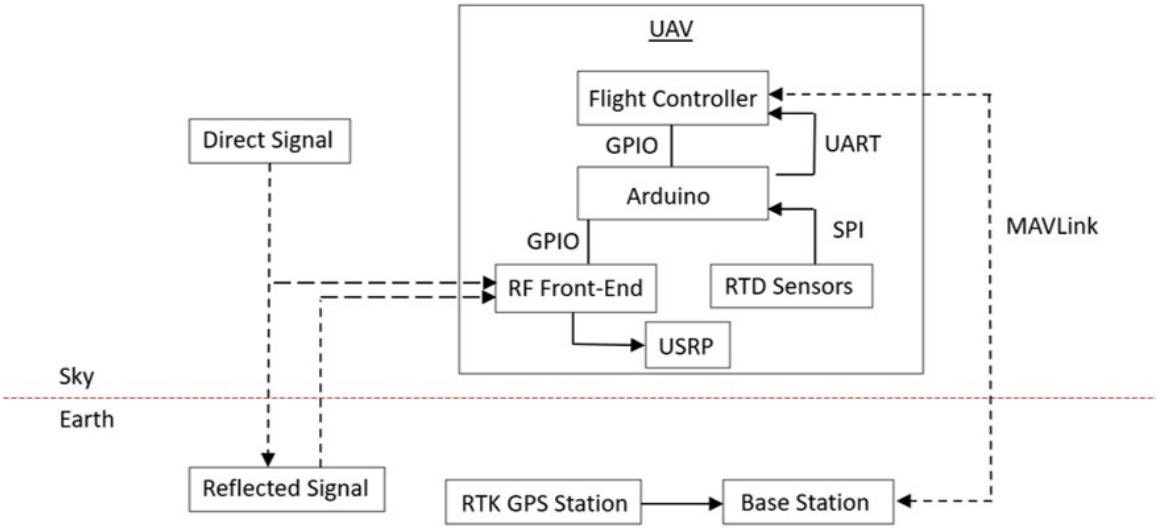


Figure 3.1.: Overall UAV Remote Sensing System Design. Signals collected by the Front-End Instrument are recorded by a USRP. The Front-End and UAV are controlled by a micro-controller combined with the base station over General Input Output pins (GPIO) and the UART protocol. The UAV is linked to the ground over a MAVLink protocol.

The system is composed of an Ettus E310 Universal Software Radio Peripheral (USRP), antennas, associated RF equipment, and a combined base station with Real Time Kinematic (RTK) GPS. The direct and reflected signals are collected with the RF front-end and USRP. The UAV is connected to a base station over a connection called MavLink, which allows telemetry to be received on the ground and commands to be sent to the flight controller on the UAV [26]. The base station segment of this system is composed of a Dell Latitude 5420 rugged laptop, which is designed with for rough use in field conditions. To aid with system calibration, Omega surface mount resistance temperature detector (RTD) sensors are placed on key RF equipment to monitor noise temperatures.

## 3.1 UAV

The UAV utilized in this experiment was a custom-ordered Tarot X6 V2.0 hexacopter from UAV Systems International. This is a heavy-lift drone capable of carrying up to a five kilogram payload. In terms of size, the UAV is approximately 1.2 meters from end-to-end. The UAV supports a flight time from 15 to 35 minutes with a distance range of up to two miles depending on the weight of the attached payload. With multiple UAV battery sets, this experiment is able to support an approximate total flight time of 45-60 minutes. Position and orientation is provided by the addition of a Drotek real time kinematic (RTK) GPS system, providing accuracy up to two and a half centimeters. The UAV is operated by an open-source Pixhawk flight controller, which makes the system easy to modify to best fulfill the needs of any experiment. Hardpoints below the drones battery deck allow for the attachment of various instruments and sensors, or in this case the RF front-end. The UAV can be flown manually in a number of different flight modes or through waypoints programmed into the system's autopilot. All parts except the motors and frame were made by American manufacturers.

(a) Tarot X6 UAV

(b) Tarot X6 UAV with RTK Station

Figure 3.2.: Tarot X6 UAV used in this project

## 3.2 Antennas

The antennas on this experiment are Taoglas Meteor FW.81 antennas. These are a flexible, omni-directional, quarter wavelength monopole whip antenna designed to receive signals at 135 MHz. Finding an ideal antenna for this project proved difficult due to the size limitations of mounting the antennas onto a UAV. As signal frequency decreases, typically a larger antenna is required to maintain the same signal to noise ratio. Due to limitations presented by the UAV platform, our antennas were severely limited in length and weight. The Taoglas antennas are 14 centimeters in length and require a 30 by 30 centimeter ground plane, which is manufactured out of lightweight 6061 aluminum.

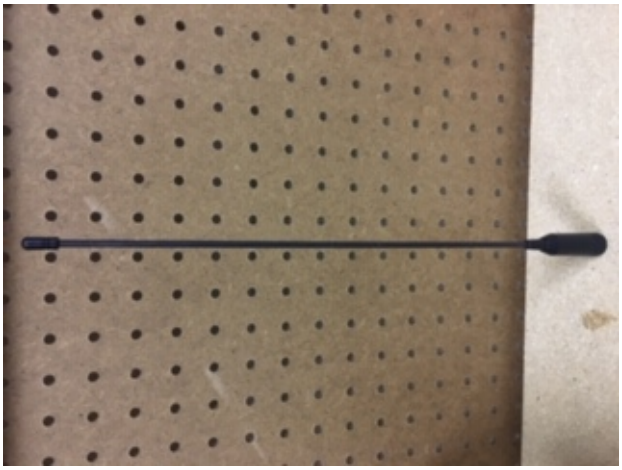

Figure 3.3.: Taoglas Quarter-Wave Monopole Antenna

Simulation of these antennas using OpenEMS software shows that the gain pattern is close to isotropic, which is the reason for the non-isolation assumption in the Signals of Opportunity model. The gain pattern is shown in Figure 3.4.

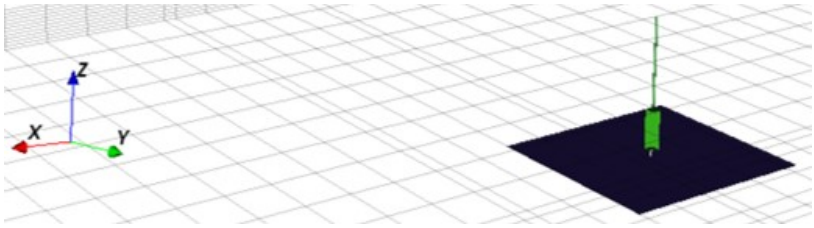


(a) Model of Antenna for Orientation

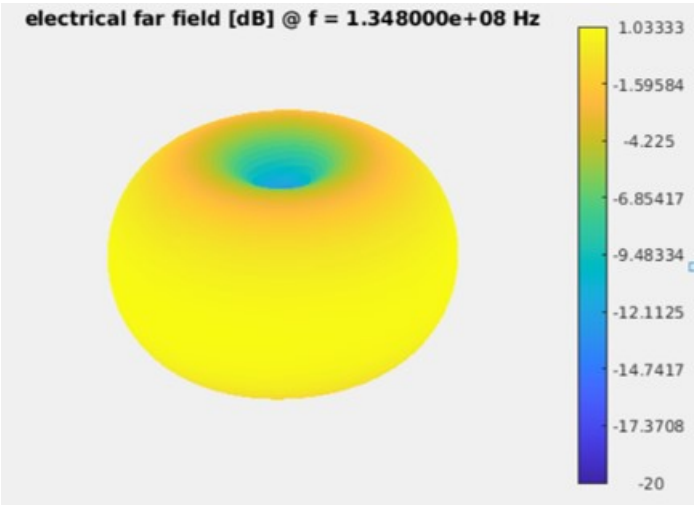


(b) Antenna Gain Pattern

Figure 3.4.: Monopole Antenna Simulation in OpenEMS

As a result, these antennas are not completely ideal for this type of project. Calibration and obtaining reflectivity is possible with non-isolation, as shown in Chapter 2 and Appendix B, but is not the desired case. Using isolated antennas would allow for easier measurements.

## 3.3 USRP

The recording device used in this experiment is the Ettus Universal Software Radio Peripheral (USRP) Software Defined Radio (SDR) model E310. This is a two-channel Multiple-Input-Multiple-Output (MIMO) Software Defined Radio capable of receiving signals with a frequency of 70 MHz up to 6 GHz with 56 MHz of bandwidth. For this experiment, the USRP records at a 1 MHz sampling rate with each

file encompassing approximately 60 seconds of recording. Each recording is a set of two files containing both a real and imaginary file, totaling 480 MB of data. Files are time and location tagged using the USRP's onboard GPS receiver.


Figure 3.5.: Ettus E310 USRP

## 3.4 RF Front-End

### 3.4.1 Design

The RF front-end is the main "guts" of the instrument in this project, allowing for system calibration that leads to reflectivity. It is enclosed in an aluminum box for better protection from radio frequency interference and is mounted to the bottom of the UAV. The front-end sits between the antennas and the USRP and is responsible for filtering and amplifying signals, as well as providing different system states for calibration. A diagram is shown in Figure 3.6.

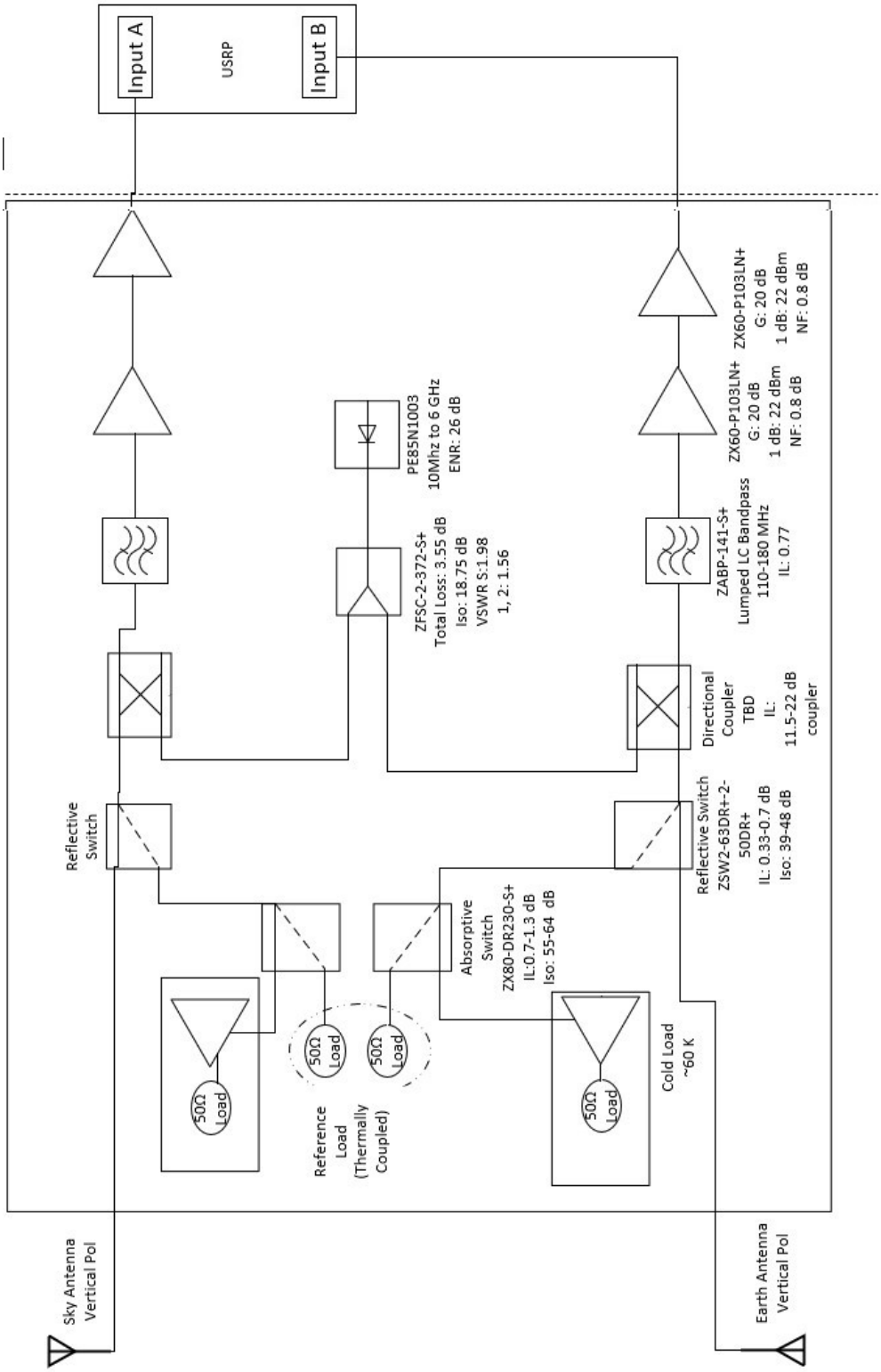


Figure 3.6.: Setup of Front-End Instrument

There are two main system paths, identical to one another in configuration. One feeds channel 1 (labeled as A in the diagram) on the USRP and the other feeds channel 2 (labeled as B). From one of the antennas, a signal is passed through a reflective switch, a bandpass filter for 110 to 180 MHz, and two 20 dB amplifiers. Noise can be injected into these system paths at any time using a noise-injection diode and directional coupler. The noise-diode provides noise with a known noise temperature. This describes what has been referred to here as the 'through' state. The reflective switches, along with two absorptive switches, can be used to switch to the cold noise and reference load states. In these cases, the signals from the antennas will be cut off and the noise from the reference and cold loads will travel through systems 1 and 2 and be measured instead. As with the through state, the noise injection diode can be on or off at any time.

The box holding the microwave equipment is constructed out of 6061 aluminum sheets screwed together onto a T-slot frame. All microwave parts are screwed into the bottom plate with lock washers to prevent loosening from vibrations during flight. The RF cabling between parts is self-assembled from RG-195 50 ohm impedance SMA cable. Power to most of the RF equipment is provided by a set of 7.4V, 1000maH Li-Po batteries. The noise diode is powered separately by a set of three rechargeable 9-volt batteries, as its voltage requirement is 28 volts as opposed to 5 volts for the rest of the components. Pictures of the completed front-end are shown in Figure 3.7. The labels are, in alphabetical order of labels respectively: absorptive switches, cold noise loads, reflective switch, power splitter, noise diode, coupler, band-pass filter, and amplifiers.

(a) Front-End Instrument Frame

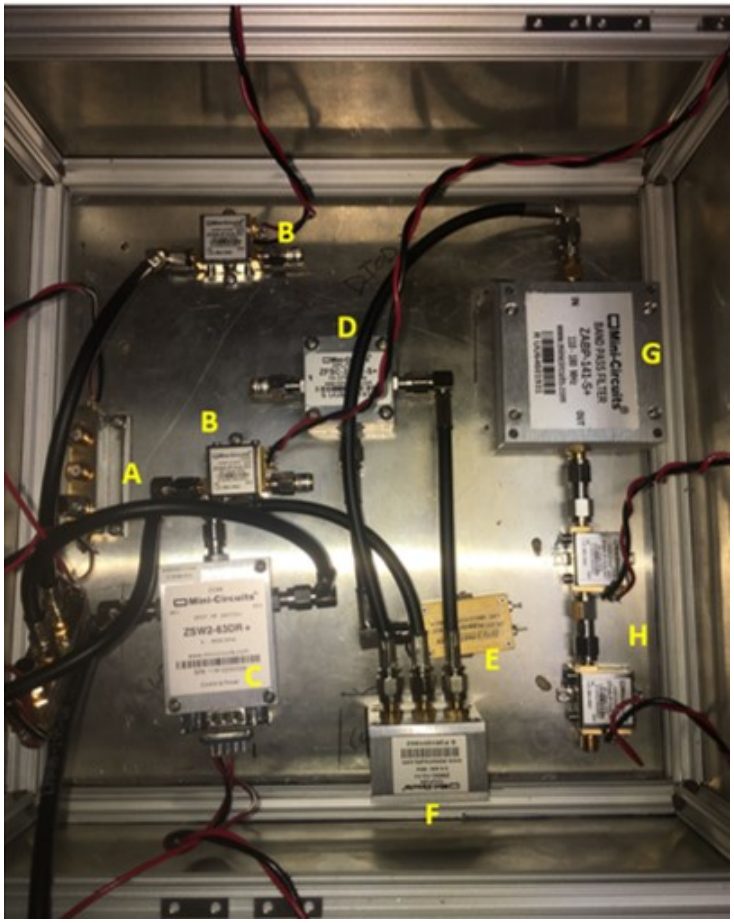


(b) RF Equipment in Front-End

Figure 3.7.: Front-End Instrument. A: Absportive Switch, B: Cold Noise Load, C: Reflective Switch, D: Splitter, E: Noise Diode, F: Coupler, G: Filter, H: Amplifier

### 3.4.2 State Switching

The system switches states in order to adequately accomplish the calibration described in Chapter 2. State switching is capable through either manual control or a preset sequence of state switching. This is accomplished through the use of a microcontroller that is connected to the Pixhawk flight controller through a Universal Asynchronous Receiver/Transmitter (UART) connection. By manipulating specific switches on the handheld transmitter, corresponding pins on the microcontroller can be triggered through the flight controller, controlling the state settings on the RF front-end. A three-option switch on the transmitter allows for manual control of the states while a spring-loaded switch allows for the triggering of the preset sequencing. An automated sequence allows for this to occur with minimal user intervention and can easily be adjusted throughout the experiment to collect a wide range of data. An example of a possible preset, automated state switching sequence is shown in Figure 3.8 .

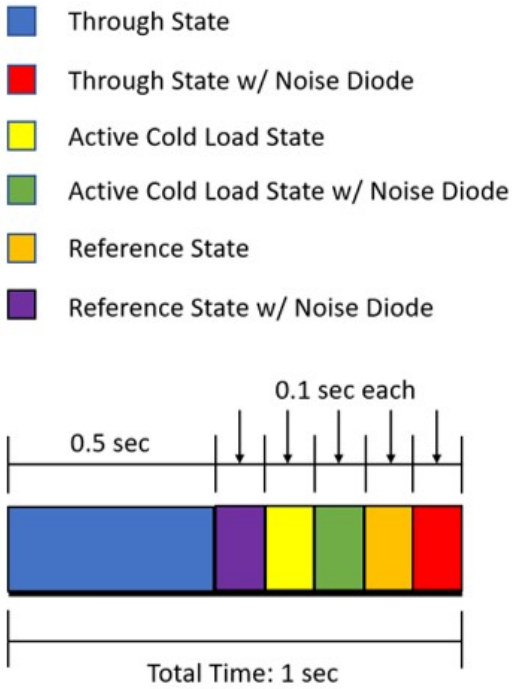


Figure 3.8.: Automated State Switching Sequence Example

This state switching can occur on the order of microseconds and milliseconds; the electrical switches used in the front-end have a switch time of between 1.6 and 2 microseconds. Switching this quickly must be conducted to meet the requirements of calibration, as amplifier gains can vary on the order of sub-seconds [27]. How quickly it changes is dependent on how quickly the system temperature changes [27]. The order of states is determined so as to make it easy to notice power changes, and in turn the state changes, when state parsing in post-processing. This is shown in Figure 3.9 for a 1 MHz bandwidth.

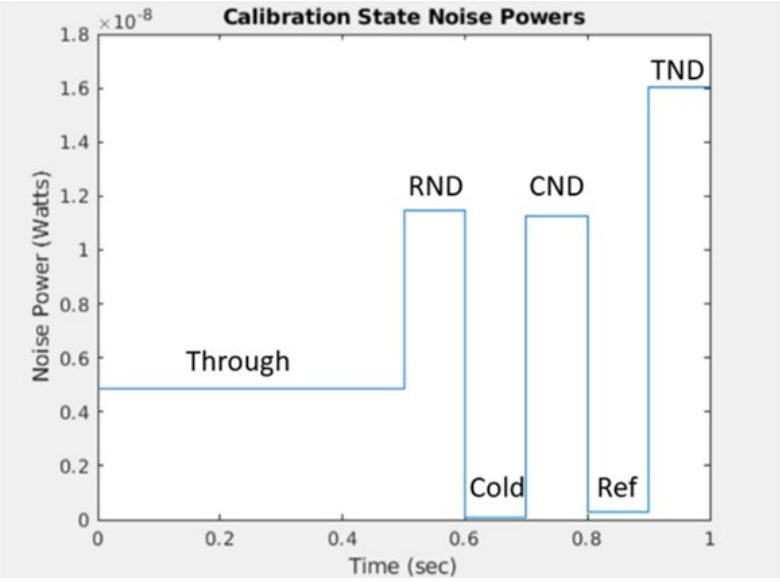


Figure 3.9.: Calibration State Noise Power Example

### 3.4.3 Mounting

The UAV has a cargo-bay type addition beneath the battery platform that has rails to assist with mounting sensors and equipment to the bottom of the drone. The front-end frame is designed small enough to be able to fit between the landing legs and attach to the bottom of this platform. One antenna will be mounted on the bottom of the front-end and the other antenna will be mounted on top of the UAV above the flight controller and GPS. A CAD diagram of this is shown in Figure 3.10.

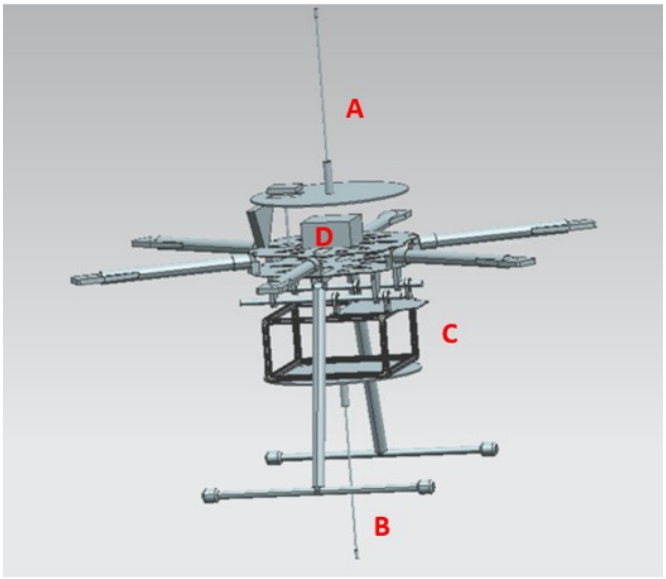


Figure 3.10.: Equipment Mounting CAD Model. A: Sky Antenna, B: Earth Antenna, C: Front-End Instrument, D: Flight Controller and Arduino

The circles beneath the antennas represent the size of the ground planes for them.

### 3.4.4 Testing and Performance

Testing of the completed RF front-end was accomplished through the use of a Field Fox spectrum analyzer. The Field Fox is capable of transmitting and receiving its own power signal, across a wide frequency spectrum, to determine the performance of a microwave system. Basic performance of the front-end was tested by conducting a scattering parameter, or S-parameter, S12 test on the three main states. Scattering, in this case, refers to the effects a component has on a signal being transmitted through a line. S-parameters are used to describe the electrical behavior of a system of components and can be used to describe properties such as gain or voltage standing wave ratio (VSWR). S-parameters are dependent on the impedance, input power, and frequency of the signal. In this case, the S-parameter is used as a representation of the frequency response of the system. While only a simple test, this would validate the construction of the front-end by testing the overall system gain and connectivity.

In an S12, the Field Fox outputs a wide-band signal at port 1 and looks to receive the signal at port 2. It then plots the ratio of power it received at port 2 to the power transmitted a port 1.

$$S_{12} = Gain(dB) = \frac{Received\ Power}{Transmitted\ Power} = \frac{Power\ Port\ 2}{Power\ Port\ 1} \tag{3.1}$$

In essence, this test provides a representation of the transfer function of the system, with the plot providing a visual example of the gain versus the signal frequency.

For all states, the input was attached to where the antennas would be and the output was attached to where the USRP would be. The input signal power for these tests was -35 dBm.

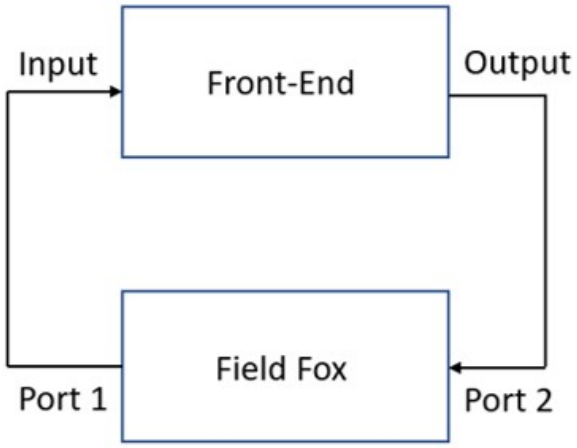


Figure 3.11.: Field Fox Test Setup

### Through State

The design of this test simulates a signal being collected by the antennas and sent through the front-end to the USRP. The purpose of this test is to evaluate both the design and construction of the front-end based on the system gain. If constructed incorrectly, the test would show a signal with lower gain than expected, meaning that signals from the "antennas" were being attenuated by poor connections. The expectation for the through state was to see a signal peak coming out of the front-end

with an approximate gain of at least 35-40 dB, as the two amplifiers in the system each are rated for about 20-25 dB in the ORBCOMM frequency range.

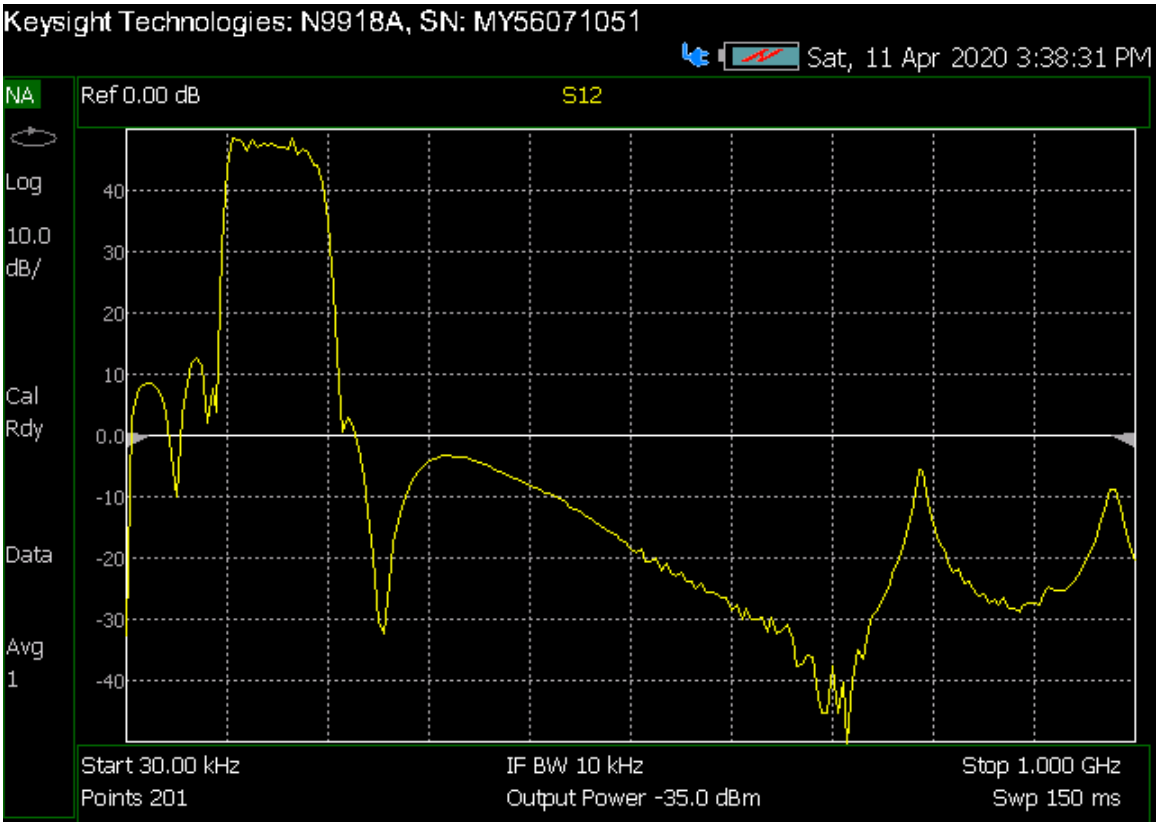


Figure 3.12.: S12 Plot of Through State

The through state S12 of the completed system shows a large peak at 45-50 dB. This means that the signal was able to pass through the front-end and there was a gain of approximately 45 dB. This matches the expectation based on the hardware used in the system. The peak is band restricted in the I-Band frequency region, which proves that the filters (115-180 MHz band-pass) inside the system were functioning properly. This test was a success and validates the general design and construction of the through state.

### Noise Load States

The setup and Field Fox configuration for the load states was the same, but the implications of the test are different. In the load states, minimal power from the antennas will make it through the system. The reflective switch cuts off the antennas and instead allows for noise from the load states to pass to the rest of the system. Because of this, an S12 measures the isolation of the load states. RF isolation is the amount a signal bleeds through a port or piece of hardware. Even though the switches "cut off" certain ports when they switch, some signal will still leak through. The isolation is amplified by the amplifiers in the front-end so the expectations for this test would be to see a peak of the isolation within the band of the system. Ideally, this isolation would be high. The results should be the same for both the reference and cold load states since the states are comprised of the same switches. Isolation should not change if the hardware is the same for each system.

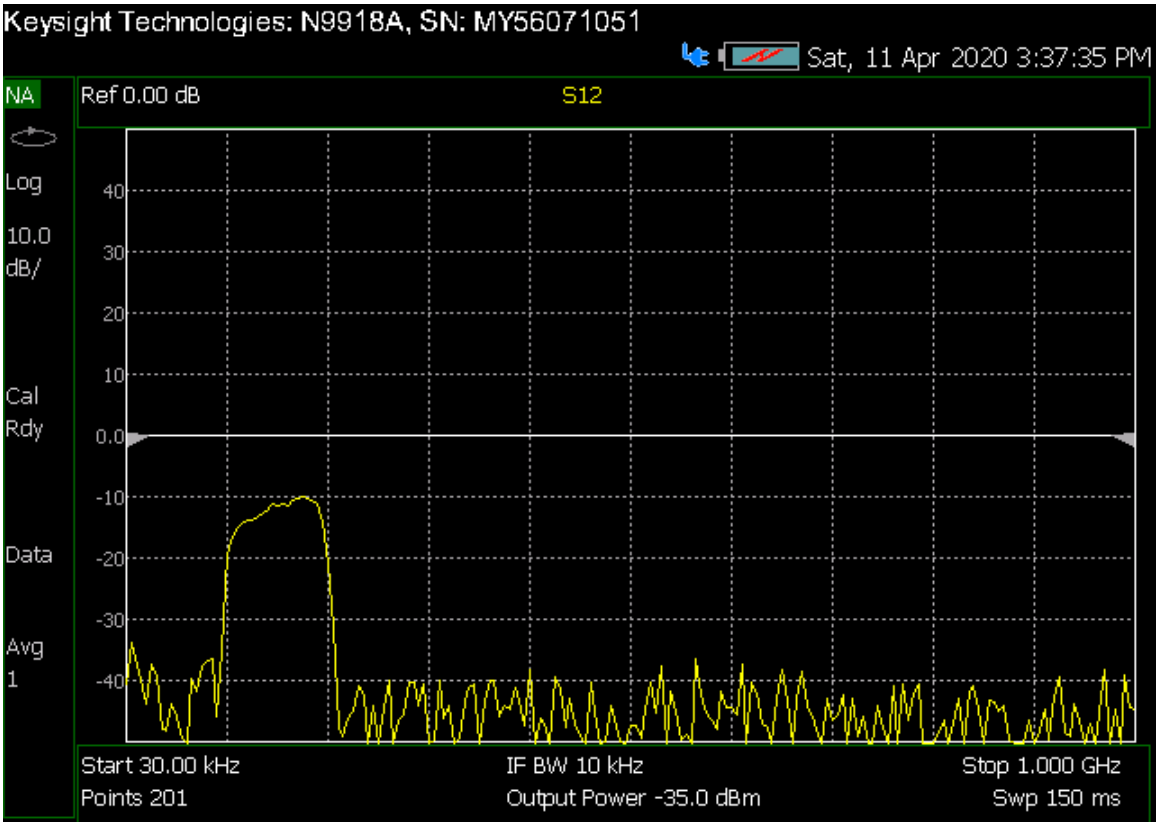


Figure 3.13.: S12 Plot of Load States

Analysis of the load states using an S12 shows a 40-50 dB peak within the filtered band of the system. Only one plot is shown here because the results of the reference and cold load states were exactly the same. These results match the expectation for isolation of the noise states. This test was also successful and validates the construction of the load states.

### Overall Performance

The following table describes the overall performance of the RF-front end.

Table 3.1.: Front-End Performance

| **Variable** | **Performance** |
|---|---|
| Gain (Theoretical) | 40-50 dB |
| Gain (Experimental) | 45 dB |
| Noise Temperature (Theoretical) | 235 K |
| Noise Figure (Theoretical) | 2.58 dB |

## 3.5 Budgets

### 3.5.1 Mass Budget

The Tarot X6 is capable of carrying up to a five kilogram payload. The front-end and remote sensing instrument in this experiment has a total mass of 3.13 kilograms, giving a margin of 1.87 kilograms. Table 3.2 breaks down the budget for this the major components of this system.

Table 3.2.: System Mass Budget

| **Part** | **Mass (kg)** | **Number** | **Total Mass (kg)** |
|---|---|---|---|
| Frame Beam Size 1 | 0.04155 | 8 | 0.33 |
| Frame Beam Size 2 | 0.01385 | 4 | 0.06 |
| T-Slot Corner | 0.00147 | 8 | 0.01 |
| Antenna | 0.04 | 2 | 0.08 |
| FE Top and Bottom Al Sheets | 0.2565 | 2 | 0.51 |
| FE Side Al Sheets | 0.0855 | 4 | 0.3 |
| **FE Frame Total Mass** | | | **1.33** |
| Reflective Switch | 0.07 | 2 | 0.14 |
| Absorptive Switch | 0.056 | 2 | 0.11 |
| Filter | 0.124 | 2 | 0.25 |
| Amplifiers | 0.023 | 6 | 0.14 |
| 50 Ohm Terminator | 0.004 | 4 | 0.016 |
| Power Splitter | 0.07 | 1 | 0.07 |
| Noise Diode | 0.0279 | 1 | 0.023 |
| Directional Coupler | 0.06 | 2 | 0.12 |
| USRP E310 | 0.375 | 1 | 0.38 |
| 7.4V LiPo Battery | 0.05 | 1 | 0.05 |
| 9V Batteries | 0.034 | 3 | 0.10 |
| RG-195 SMA Cable | 0.019 | 21 | 0.40 |
| **Total Mass (kg)** | | | **3.13** |

### 3.5.2 Power Budget

The main power supply for the instrument is a TATTU 7.4V, 1000mAH airsoft LiPo battery. Because the noise diode's voltage requirement is much higher than the rest of the components, it is powered separately by a set of rechargeable LP 9V batteries. Table 3.3 and Table 3.4 show the power requirements and battery specifications for this experiment.

Table 3.3.: System Power Requirements

| Component | Voltage (V) | Current (mA) | Total Average Power (mW) |
|---|---|---|---|
| Absorptive Switch (x2) | 5 | 0.5 (Supply); 0.5 (Control per pin) | 7.5 |
| Reflective Switch (x2) | 5 | 0.15 (Supply); 0.04 (Control) | 1.688 |
| Amplifiers (x6) | 5 | 120 | 2640 |
| USRP | 5 | 400 | 2000 |
| Arduino | 5 | 20 | 100 |
| Noise Diode | 28 | 25 | 700 |

Table 3.4.: Power Supply Specifications

| Battery | Voltage (V) | Capacity (mAh) | Power (mWh) | Time (Hrs) |
|---|---|---|---|---|
| Main Power Supply - LiPo | 7.4 | 1000 | 7400 | 1.59 |
| Noise Diode Power Supply | 28 | 600 | 16200 | 23.14 |

At full charge, the main power supply can run for approximately an hour and a half while the noise diode power supply can run for almost an entire day. Even though the voltage supplied by the 9Vs is slightly under the listed 28V, the noise diode is capable of running between 22 and 30 volts. Because this experiment has a total flight time of 45-60 minutes (three flights), a front-end power supply of 1.5 hours is sufficient.

### 3.5.3 Link Budget

The link budget for this experiment estimates the signal-to-noise ratio from an ORBCOMM satellite as $C/N_0$. This is an important aspect to keep in mind when designing the instrument because a poor link budget will make it difficult to measure

reflectivity. The hardware in the system affects the overall noise figure and lossy components will negatively impact calibration and soil moisture retrieval.

The link budget is found by first calculating the received signal power at the antenna $P_r$:

$$P_r(dB) = P_t + G_t - L_0 - L_A - L_P + G_r = EIRP - L_0 - L_A - L_P \tag{3.2}$$

Table 3.5.: Link Budget Terms

| | |
|---|---|
| $P_t$ | Transmiter Power |
| $G_t$ | Transmitter Gain |
| $L_0$ | Path Loss |
| $L_A$ | Atmospheric Loss |
| $L_P$ | Polarization Loss |
| $G_r$ | Receiver Gain |
| $\sigma$ | Boltzmann Constant |
| $T_{Sys}$ | System Noise Temperature |
| $B$ | Bandwidth |

The transmitter terms are typically combined into one term known as the Effective Isentropic Radiated Power (EIRP). Path loss, the losses due to transmission through space over long distance, is related to the wavelength and distance between the transmitter and receiver:

$$L_0(dB) = 10\log_{10}\left(\frac{\lambda^2}{16\pi^2 R^2}\right) \tag{3.3}$$

The signal-to-noise ratio is found by combining the power at the antenna with the gains and losses of the receiver:

$$C/N_0(dB) = P_r - \sigma - T_{sys} - B \tag{3.4}$$

The total $C/N_0$ for this experiment is 28 dB for the skyward facing antenna and 21.8 dB for the earth facing antenna. The full link budget is broken down in Table 3.6. The

polarization and atmospheric losses are taken from ORBCOMM documentation [28]. All others are calculated.

Table 3.6.: ORBCOMM Link Budget

| **System/Effect** | | **Units** |
|---|---|---|
| Spacecraft EIRP | 12 | dBW |
| Ground Antenna Gain | 0 | dBi |
| Path Loss | -140.21 | $dBm^2$ |
| Atmospheric Loss | 0.2 | dB |
| Polarization Losses | 4.1 | dB |
| Reflection Coefficient | 0.5 | |
| **Power at Antenna Sky** | **-132.51** | **dBW** |
| **Power at Antenna Earth** | **-135.52** | **dBW** |
| Boltzmann Term | -228.60 | (dBW*Hz)/K |
| Sky Noise Temp Term | 24.08 | dB/K |
| Earth Noise Temp Term | 27.21 | dB/K |
| Bandwidth Term | 43.98 | dBHz |
| **C/No Sky** | **28.03** | **dB** |
| **C/No Earth** | **21.89** | **dB** |

The system noise temperature is found by combining the antenna noise temperature with the front-end system noise temperature.

$$T_{Sys} = T_{Ant} + T_{Eq} \tag{3.5}$$

The front-end's equivalent noise temperature is calculated through the use of Friis' formula, which states that the equivalent noise factor of a cascading RF system is:

$$F_{Eq} = F_1 + \frac{(F_2 - 1)}{G_1} + \frac{(F_3 - 1)}{G_1 G_2} + \frac{(F_4 - 1)}{G_1 G_2 G_3} + ..... \tag{3.6}$$

A component's noise factor, $F$, is the linear equivalent of its noise figure in dB. The gain, $G$, of components that do not provide an inherent gain (ie. amplifiers) is found by taking their noise figure as a negative gain (a positive loss is a negative gain) and converting to linear units. Table 3.7 outlines the noise information for the equipment used in each of the identical systems in the front-end.

Table 3.7.: System Noise Figures

| **Component** | **Noise Figure (dB)** | **Noise Factor (non-dB)** | **"Gain" (non-dB)** | **Noise Temperature (K)** |
|---|---|---|---|---|
| Reflective Switch | 0.33 | 1.08 | 0.93 | 22.90 |
| Coupler | 0.65 | 1.16 | 0.86 | 46.82 |
| Filter | 0.8 | 1.20 | 0.83 | 58.66 |
| Amplifier (Gain $\sim$ 23dB) | 0.8 | 1.20 | 199.53 | 58.66 |
| Amplifier | 0.8 | 1.20 | 199.53 | 58.66 |
| USRP | 8 | 6.31 | 0.16 | 1539.78 |

The total noise figure of the front-end, calculated using Equation 3.6, is 2.584 dB, which corresponds to an equivalent noise temperature of 235.790 K. The antenna noise temperature is estimated as 20 K and 290 K, respectively, for skyward and Earth facing.

# 4. GROUND SUPPORT

Flights are planned and supported using a combination of ground control software and specular point mapping software. Specular points are the locations of where the measurement is being taken; therefore, knowing their location is vital to remote sensing projects. The specular mapping assists in determining waypoints for the UAV to fly to in order to receive measurements over the desired areas or obtaining specular points from an already flown path. The ground control software assists with managing the UAV, its flight modes and autopilot, and telemetry.

## 4.1 Ground Control Software

The base station runs an autopilot and ground control software called ArduPilot Mission Planner. ArduPilot is an open-source program that combines autopilot, data analysis, and simulation tools in one. Mission Planner is ArduPilot's first and most widely supported ground control station (GCS). Upon system setup, the GCS makes a remote connection with the Pixhawk flight controller on the UAV over a protocol known as MavLink. The RTK GPS comprises the third connection of the ground station "triangle", with many Mission Planner features restricted without a strong GPS lock. An example of the Mission Planner interface, with GPS showing an accurate location in Armstrong Hall, is shown by Figure 4.1.

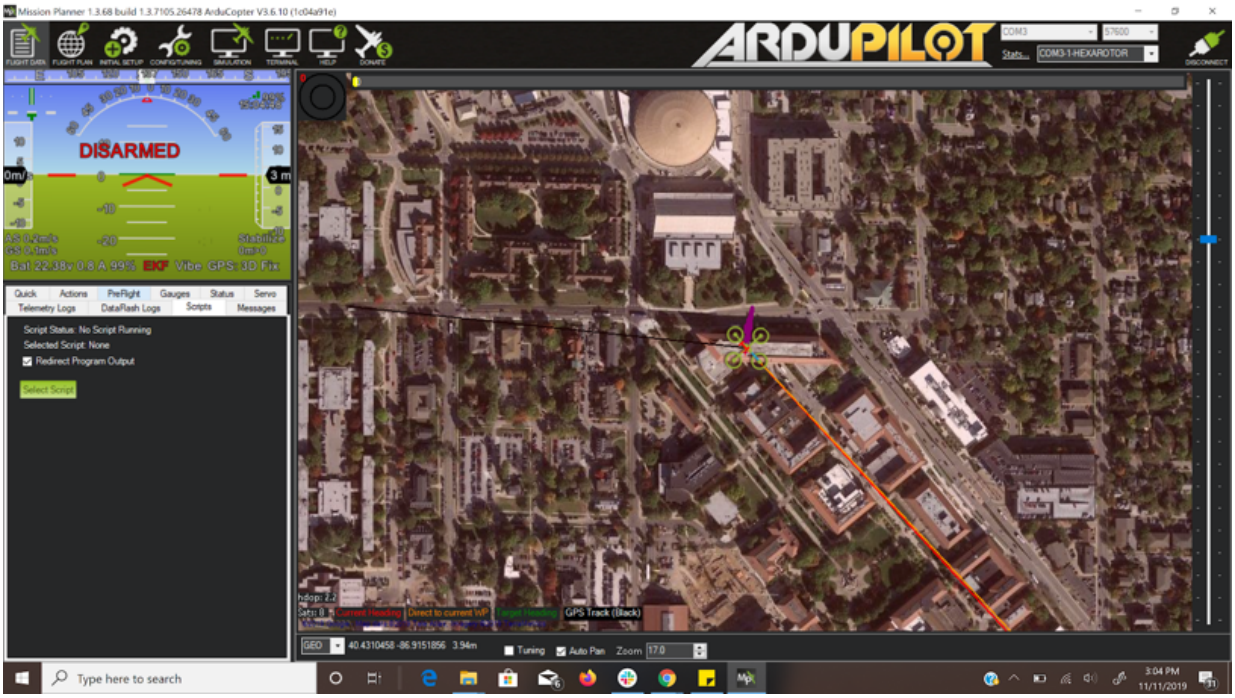


Figure 4.1.: Mission Planner Interface

The GCS, in conjunction with the Drotek RTK GPS, allows for precise planning and control of flights when used. Flights can be pre-programmed with waypoints using the autopilot and flown by the drone without user intervention. In both autopilot and manual control modes, the GCS monitors the state of the drone to include battery levels, positioning, system configuration, etc. All telemetry is sent over MavLink and can be saved and analyzed using the GCS. For this system, temperature sensor data from the RF front-end is included in this telemetry as well for easy access.

## 4.2 Specular Point Mapping

For this project, a specular point mapping program was created in MATLAB. This program takes a given GPS location for the UAV receiver and generates a KML file for use with Google Earth, plotting specular points and fresnel zones. The program is modular in terms of which signal can be used and requires an up-to-date two-line element (TLE) file for whichever signal of opportunity is used. Because the specular

point is not always, and most often not, simply beneath the UAV, this mapping program is a powerful tool for ensuring that the flight path of the drone actually corresponds to the area in question. Through iteration, a flight path can be found that results in specular points over the area of interest.

### 4.2.1 Algorithm

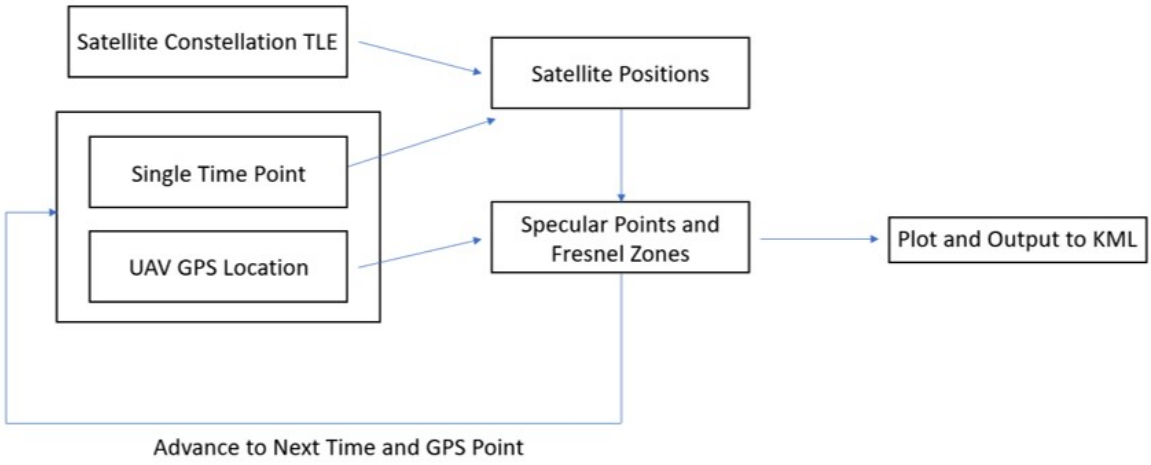


Figure 4.2.: Specular Mapping Algorithm

Specular points and fresnel zones are calculated for discrete points in time and GPS location. For each single point, a TLE for a given satellite constellation is inputted to the program. Most TLEs are easily obtainable online. This project used N2Y0. The positions of each satellite can be calculated using the TLE. The program created for this project utilizes an SPG4 toolbox from the MATLAB website, which calculates the geodetic coordinates and altitude of each satellite from the TLE and given time point [29]. Next, the specular points are calculated based off of the geometry between the satellite and receiver location.

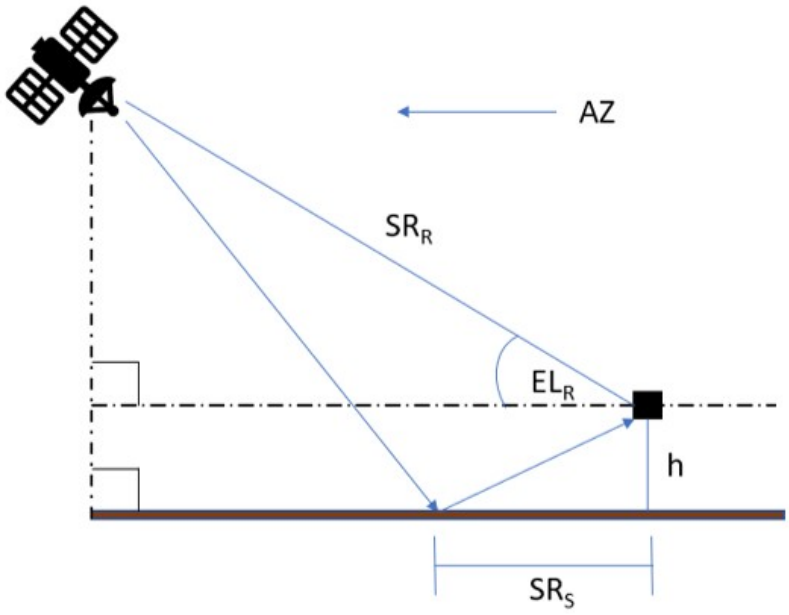


Figure 4.3.: Specular Mapping Geometry

Table 4.1.: Specular Mapping Variables

| **Variable** | **Definition** |
|---|---|
| $AZ_R$ | Azimuth between Reference Point and Satellite |
| $AZ_S$ | Azimuth between Specular Point and Ground beneath Reference Point |
| $EL_R$ | Elevation Angle between Reference Point and Satellite |
| $EL_S$ | Elevation Angle between Specular Point and Ground beneath Reference Point |
| $SR_R$ | Distance between Reference Point and Satellite |
| $SR_S$ | Distance between Specular Point and Ground beneath Reference Point |
| $h$ | Altitude |
| $\phi$ | Latitude |
| $\lambda$ | Longitude |

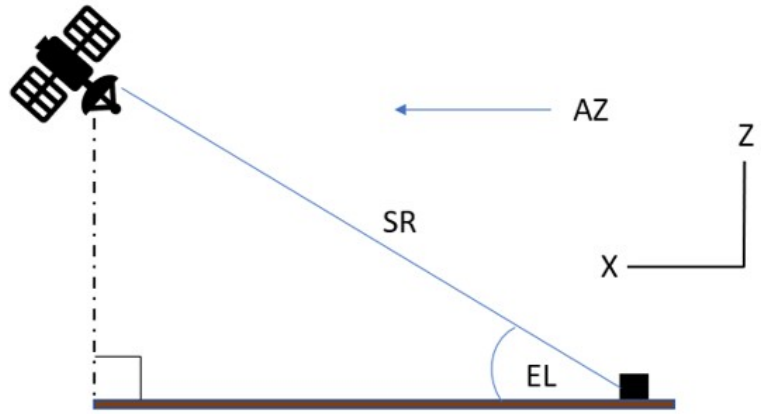


(a) Azimuth, Elevation, Slant Range (AER) Reference Frame

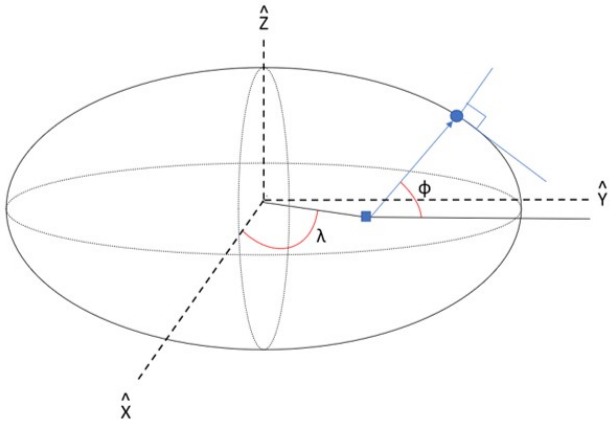


(b) Geodetic Reference Frame

Figure 4.4.: Specular Mapping Reference Frames

First, the GPS coordinates (latitude, longitude, altitude) of the UAV are used to find the azimuth, elevation, and range to the satellite. The azimuth, elevation angle, and slant range (AER) from the receiver to the satellite $(AZ_R, EL_R, SR_R)$ are calculated using the geodetic2aer function from the MATLAB mapping toolbox [30]. This function outputs the azimuth, elevation angle, and slant range between a ground location and a satellite given the latitude, longitude, and altitude of the two points. Next, the

azimuth, elevation, and slant range of each specular point are found with respect to the ground beneath the UAV reference point:

$$AZ_S = AZ_R \tag{4.1}$$

$$EL_S = 0 \tag{4.2}$$

$$SR_S = \frac{h}{\tan(EL_R)} \tag{4.3}$$

The azimuth, elevation angle, and slant range of the specular point, with respect to the ground beneath the UAV location, are converted back into a geodetic latitude, longitude, and altitude using the aer2geodetic in MATLAB. This function converts azimuth, elevation angle, and range into a latitude, longitude, and altitude given a GPS coordinate as reference [31]. The altitude of the specular point is simply the ground elevation of the reference location.

To convert the azimuth, elevation, and range of the specular point to geodetic coordinates, they are first transformed into the Cartesian ENU frame:

$$X_{East} = SR_S \cos(EL_S) \sin(AZ_S) \tag{4.4}$$

$$Y_{North} = SR_S \cos(EL_S) \cos(AZ_S) \tag{4.5}$$

$$Z_{Up} = SR_S \sin(EL_S) \tag{4.6}$$

Next, the offset from the original reference ground location in the ECEF frame is found:

$$dx = \cos(\lambda_{Ref})(\cos(\phi_{Ref})Z_{Up} - \sin(\phi_{Ref})Y_{North}) - \sin(\lambda_{Ref})X_{East} \tag{4.7}$$

$$dy = \sin(\lambda_{Ref})(\cos(\phi_{Ref})Z_{Up} - \sin(\phi_{Ref})Y_{North}) + \cos(\lambda_{Ref})X_{East} \tag{4.8}$$

$$dz = \sin(\phi_{Ref})Z_{Up} + \cos(\phi_{Ref})Y_{North} \tag{4.9}$$

The offset is added to the geodetic coordinates of the ground beneath the reference location transformed into the ECEF frame:

$$X_{Spec} = \left( \frac{a_{Earth}}{\sqrt{1 - ecc_{Earth} \sin^2(\phi_{Ref})}} + Alt_{Ground} \right) \cos(\phi_{Ref}) \cos(\lambda_{Ref}) + dx \quad (4.10)$$

$$Y_{Spec} = \left( \frac{a_{Earth}}{\sqrt{1 - ecc_{Earth} \sin^2(\phi_{Ref})}} + Alt_{Ground} \right) \cos(\phi_{Ref}) \sin(\lambda_{Ref}) + dy \quad (4.11)$$

$$Z_{Spec} = \left( \frac{a_{Earth}(1 - ecc_{Earth}^2)}{\sqrt{1 - ecc_{Earth} \sin^2(\phi_{Ref})}} + Alt_{Ground} \right) \sin(\phi_{Ref}) \quad (4.12)$$

The coordinates for the specular point in ECEF are then transformed into geodetic:

$$\beta = \arctan \left( \frac{Z_{Spec}}{(1 - Flatness_{Earth}) \sqrt{X_{Spec}^2 + Y_{Spec}^2}} \right) \quad (4.13)$$

$$\phi_{Spec} = \arctan \left( \frac{Z_{Spec} + b_{Earth} ecc'^2_{Earth} \sin^3(\beta)}{\sqrt{X_{Spec}^2 + Y_{Spec}^2} - a_{Earth} ecc_{Earth} \cos^3(\beta)} \right) \quad (4.14)$$

$$\lambda_{Spec} = \arctan \left( \frac{Y_{Spec}}{X_{Spec}} \right) \quad (4.15)$$

$$h_{Spec} = h_{Ground} \quad (4.16)$$

The Fresnel zone around each specular point is an ellipse with semi-major and semi-minor axes of size:

$$a = \frac{\sqrt{h\lambda \sin(EL_R)}}{\sin(EL_R)^2} \quad (4.17)$$

$$b = \frac{\sqrt{h\lambda \sin(EL_R)}}{\sin(EL_R)} \quad (4.18)$$

The coordinates of Fresnel zones are calculated by generating a set of real and imaginary coordinates in the ENU frame based off of the Fresnel zone size and specular

point location. To generate a full ellipse, the points are calculated using an area variable $f_p t$, which is an equally spaced array from 0 to $2\pi$.

$$y_{Fresnel} = (b\cos(f_p t) + ja\sin(f_p t))e^{-jAZ_{S(rad)}} \tag{4.19}$$

The Fresnel zone coordinates are then transformed from the ENU frame into geodetic coordinates using the same method in Equations 4.4-4.16 where:

$$X_{FresnelENU} = Real(y_{Fresnel}) \tag{4.20}$$

$$Y_{FresnelENU} = Imag(y_{Fresnel}) \tag{4.21}$$

$$Z_{FresnelENU} = 0 \tag{4.22}$$

and the geodetic coordinates of the specular points are used in place of the geodetic coordinates of the reference location.

The program then updates to the next time point and repeats this process until there are no more data points. Once complete, it uses the Google Earth toolbox from MATLAB to generate a KML file that plots the receiver positions, specular points, and Fresnel zones. The program can also plot boxes or shapes to highlight certain areas, such as specific fields, if given GPS coordinates for an outline.

### 4.2.2 Examples

Figure 4.5 shows an example output for ORBCOMM specular points over a field at Purdue's Martell Forest for a single point in time.

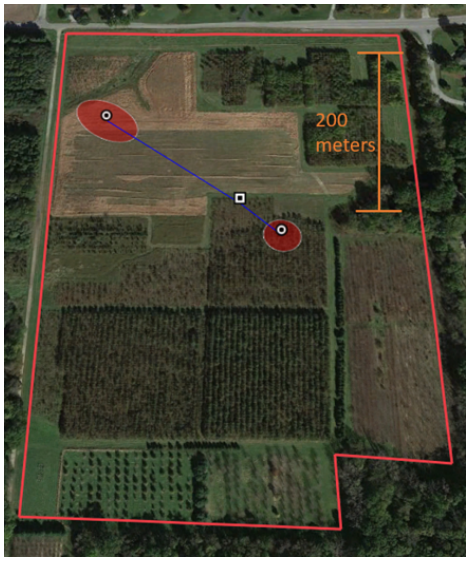


Figure 4.5.: One Reference Point, Two Satellites, 400 ft Altitude, Martell Forest

Squares denote the position of the UAV/receiver and circles denote the specular points. The ovals represent the Fresnel zones for each specular point. The red box outlines the boundary of the field at Martell where flights are planned to take place. Blue lines link a specular point to its corresponding UAV reference point.

Figure 4.6 provides an example for a plot with multiple time points, in this specific case three.

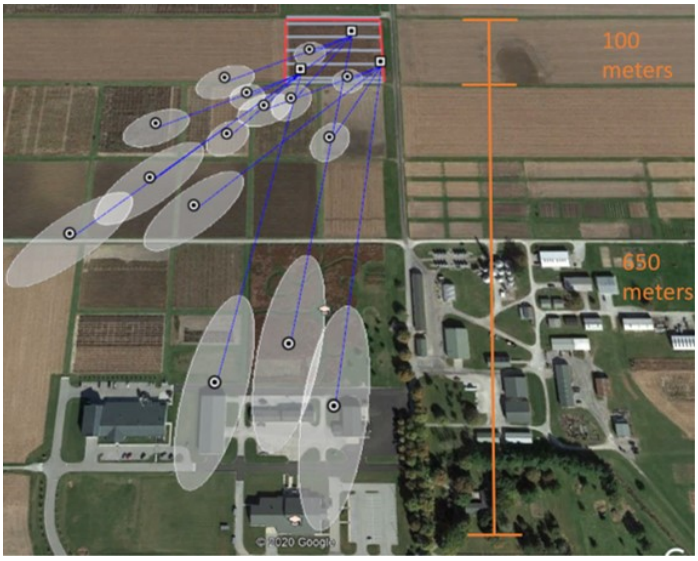


Figure 4.6.: Three Reference Points, Four Satellites, 10 sec apart, 400 ft Altitude, Purdue ACRE

This plot provides a good example of how the specular points vary widely for this project. This is because of the rapid nature of movement between the UAV and the satellites. ORBCOMM satellites are in LEO, which will result in a wider variation of specular points than a satellite in GEO. Even though numerous specular points are present, only a few are over the desired area. Figure 4.7, shows the effect of altitude change. This plot was create using three points at the same location but at altitudes of 20 meters, 80 meters, and 110 meters.

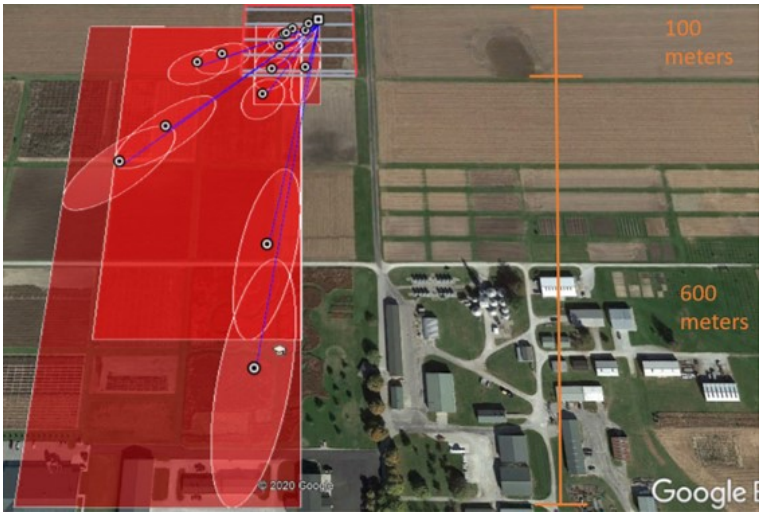


Figure 4.7.: Three Reference Points, Five Satellites, 65, 260, and 400 ft Altitude, Purdue ACRE

The same variation still exists because of the LEO satellites, but the effect of altitude is easy to see. Flying at a lower altitude results in specular points closer to the UAV than flying at higher altitude.

The final examples shown provide a visual on the impact time alone has on specular points. Over longer periods time, the large number of satellites guarantees that the specular points will widely cover the desired area. In these plots, the reference location stays the same for a period of time where each data point represents a minute in time. Figure 4.8a covers a time of 5 minutes and Figure 4.8b covers a time of 20 minutes.

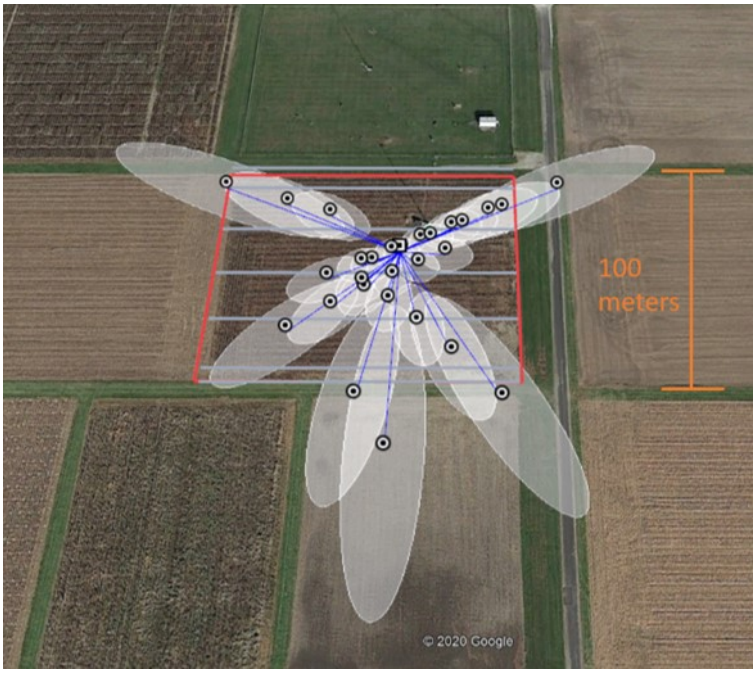


(a) Constant Location, 5 Satellites, 5 minute duration, 1 minute apart, Purdue ACRE

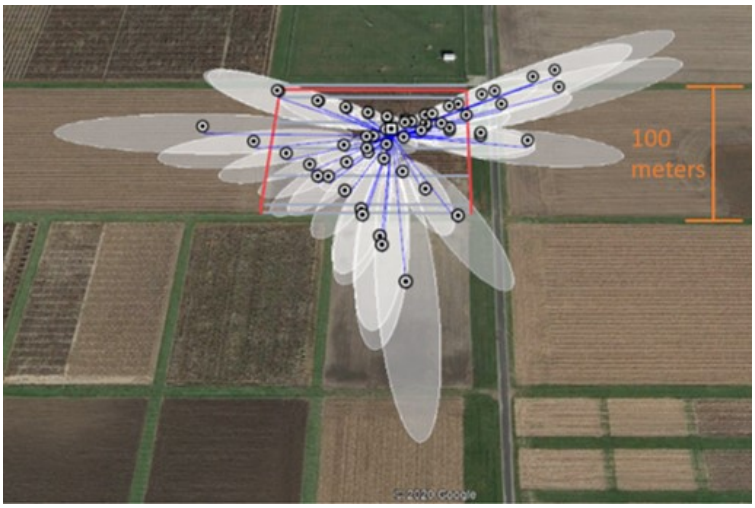


(b) Constant Location, 5+ Satellites, 20 minute duration, 1 minute apart, Purdue ACRE

Figure 4.8.: Specular Points over Time

To provide a better sense of time effects, Figure 4.9 shows the specular points from specific satellites over a short period of three minutes with a constant reference location. At an altitude of only 65 feet or 20 meters, the specular points do not move

as drastically but the figures provide of clearer image of how the movement of the satellites alone impacts the location of the specular points. The first image contains the specular points of one satellite while the second contains two satellites. Figure 4.9b shows an interesting case where one of the satellites has come into view halfway through the prediction period, as seen by the two specular points instead of three.

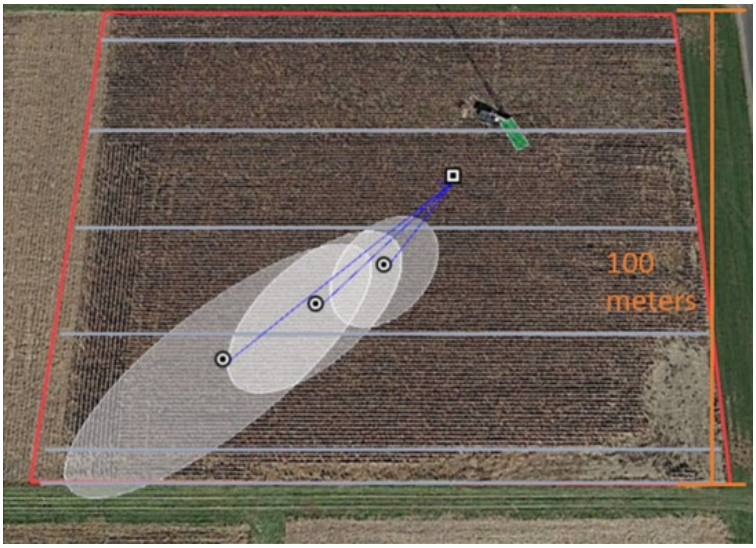


(a) Constant Location, One Satellite, 65 ft Altitude, 3 minute duration, 1 minute apart, Purdue ACRE

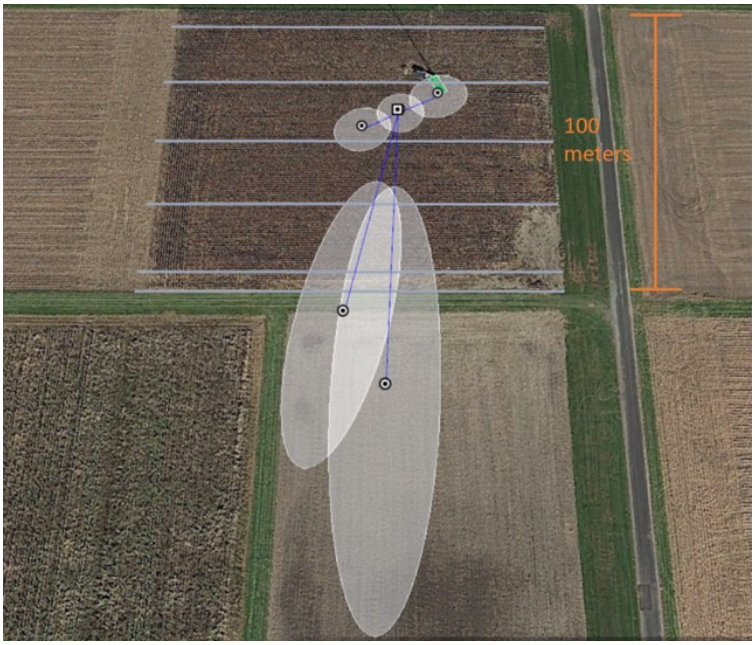


(b) Constant Location, Two Satellites, 65 ft Altitude, 3 minute duration, 1 minute apart, Purdue ACRE

Figure 4.9.: Specular Points over Time

# 5. CONCLUSION

A remote-sensing instrument for I-Band Signals of Opportunity was designed and assembled for attachment to a UAV. Using signals from the ORBCOMM communication constellation, this experiment is to provide a highly mobile and accurate platform for improvements in the remote sensing of root zone soil moisture. I-Band reflectometry offers numerous benefits over current soil moisture remote sensing techniques, the largest of which is a substantial increase in total sensing depth.

Future tasks for this project will finalize the construction of the overall system, with focus on mounting the front-end and other equipment to the UAV. The USRP recording programs should be updated for ease of use with the final system. Once mounted, testing should be conducted to ensure the proper flight dynamics of the UAV. Initial flights should focus on the proof-of-concept for the system. Combined flights over water and land could provide adequate calibration of the front-end using techniques described in chapter four. Once properly calibrated, the system can be used for data collection campaigns over Purdue's Martell Forest and Purdue ACRE.

Another area of improvement that remains is the antennas. The Taoglas antennas used in this project do not offer an ideal gain pattern for collecting ORBCOMM signals in an isolated fashion. Measuring reflectivity would be easier and more accurate with isolated antennas. Custom designed antennas, such as the X-Wing design from Myers Engineering International, should be considered as replacements to improve both link budget and post-processing.

# REFERENCES

# REFERENCES


[1] PH Gleick and S Schneider. Encyclopedia of climate and weather. *Water Resources*, 2:817–823, 1996.

[2] World Meteorological Organization. Essential climate variables. Available at: `https://public.wmo.int/en/programmes/global-climate-observing-system/essential-climate-variables`.

[3] National Aeronautics and Space Administration. Responding to the challenge of climate and environmental change:nasas plan for a climate-centric architecture for earth observations and applications from space. Technical report, National Aeronautics and Space Administration, Washington, DC, 2010.

[4] National Academies of Sciences, Engineering, and Medicine. Thriving on our changing planet: A decadal strategy for earth observation from space. Technical report, The National Academies Press, Washington, DC, 2018.

[5] Marco L Carrera, Bernard Bilodeau, Stéphane Bélair, Maria Abrahamowicz, Albert Russell, and Xihong Wang. Assimilation of passive l-band microwave brightness temperatures in the canadian land data assimilation system: Impacts on short-range warm season numerical weather prediction. *Journal of Hydrometeorology*, 20(6):1053–1079, 2019.

[6] Liao-Fan Lin, Ardeshir M Ebtehaj, Jingfeng Wang, and Rafael L Bras. Soil moisture background error covariance and data assimilation in a coupled land-atmosphere model. *Water Resources Research*, 53(2):1309–1335, 2017.

[7] Justin A Covert. Comparison of cloud systems simulated with two-dimensional and three-dimensional cloud resolving models. Iowa State University, 2019. Available at: `https://lib.dr.iastate.edu/etd/17660/`.

[8] National Oceanic and Atmospheric Administration. Gcos land ecv - above ground biomass. Available at: `https://www.ncdc.noaa.gov/gosic/gcos-essential-climate-variable-ecv-data-access-matrix/gcos-Land-ecv-above-ground-biomass`.

[9] John D Bolten, Wade T Crow, Xiwu Zhan, Thomas J Jackson, and Curt A Reynolds. Evaluating the utility of remotely sensed soil moisture retrievals for operational agricultural drought monitoring. *IEEE Journal of Selected Topics in Applied Earth Observations and Remote Sensing*, 3(1).

[10] Mark E Hawley, Thomas J Jackson, and Richard H McCuen. Surface soil moisture variation on small agricultural watersheds. *Journal of Hydrology*, 62(1-4):179–200, 1983.

[11] Lionel Duband. Space cryocooler developments. *Phys. Procedia*, 67:1–10, 2015.

[12] Dara Entekhabi, Eni G Njoku, Peggy E O'Neill, Kent H Kellogg, Wade T Crow, Wendy N Edelstein, Jared K Entin, Shawn D Goodman, Thomas J Jackson, Joel Johnson, et al. The soil moisture active passive (smap) mission. *Proceedings of the IEEE*, 98(5):704–716, 2010.

[13] T Schmugge, P Gloersen, Tom Wilheit, and F Geiger. Remote sensing of soil moisture with microwave radiometers. *Journal of Geophysical Research*, 79(2):317–323, 1974.

[14] Eni G Njoku and Dara Entekhabi. Passive microwave remote sensing of soil moisture. *Journal of hydrology*, 184(1-2):101–129, 1996.

[15] Stephen J Katzberg and James L Garrison Jr. Utilizing gps to determine ionospheric delay over the ocean. NASA Technical Report, 1996. Available at `https://ntrs.nasa.gov/search.jsp?R=19970005019`.

[16] Dallas Masters, Penina Axelrad, and Stephen Katzberg. Initial results of land-reflected gps bistatic radar measurements in smex02. *Remote sensing of environment*, 92(4):507–520, 2004.

[17] Hyunglok Kim and Venkat Lakshmi. Use of cyclone global navigation satellite system (cygnss) observations for estimation of soil moisture. *Geophysical Research Letters*, 45(16):8272–8282, 2018.

[18] CC Chew and EE Small. Soil moisture sensing using spaceborne gnss reflections: Comparison of cygnss reflectivity to smap soil moisture. *Geophysical Research Letters*, 45(9):4049–4057, 2018.

[19] Maria Paola Clarizia, Nazzareno Pierdicca, Fabiano Costantini, and Nicolas Floury. Analysis of cygnss data for soil moisture retrieval. *IEEE Journal of Selected Topics in Applied Earth Observations and Remote Sensing*, 12(7):2227–2235, 2019.

[20] Rashmi Shah, James L Garrison, Alejandro Egido, and Giulio Ruffini. Bistatic radar measurements of significant wave height using signals of opportunity in l-, s-, and ku-bands. *IEEE Transactions on Geoscience and Remote Sensing*, 54(2):826–841, 2015.

[21] Soon Chye Ho, Rashmi Shah, James L Garrison, Priscilla N Mohammed, Adam Schoenwald, Randeep Pannu, and Jeffrey R Piepmeier. Wideband ocean altimetry using ku-band and k-band satellite signals of opportunity: proof of concept. *IEEE Geoscience and Remote Sensing Letters*, 16(7):1012–1016, 2019.

[22] James Garrison, Yao Cheng Lin, Benjamin Nold, Jeffrey R. Piepmeier, Manuel A. Vega, Matthew Fritts, Cornelis F.Du Toit, and Joseph Knuble. Remote sensing of soil moisture using P-band signals of opportunity (SoOp): Initial results. In *International Geoscience and Remote Sensing Symposium (IGARSS)*, volume 2017-July, pages 4158–4161, 2017.

[23] Dylan Boyd, Mehmet Kurum, James Garrison, Benjamin Nold, Garett Pignotti, Jeffrey Piepmeier, Manuel Vega, and Rajat Bindlish. Probing soil moisture up to root-zone by using multiple signals of opportunity. In *2018 International Conference on Electromagnetics in Advanced Applications (ICEAA)*, pages 206–209. IEEE, 2018.

[24] National Telecommunications and Information Administration. United states frequency allocations: The radio spectrum. Available at : https://www.ntia.doc.gov/files/ntia/publications/january_2016_spectrum_wall_chart.pdf.

[25] Neil R Peplinski, Fawwaz T Ulaby, and Myron C Dobson. Dielectric properties of soils in the 0.3-1.3-ghz range. *IEEE transactions on Geoscience and Remote sensing*, 33(3):803–807, 1995.

[26] MAVLink. Mavlink developer guide. Available at: https://mavlink.io/en/.

[27] Fawwaz T. Ulaby and David G. Long. *Microwave Radar and Radiometric Remote Sensing*. University of Michigan Press, 2013. Chapter 7, Page 280.

[28] ORBCOMM. Orbcomm system overview. Technical Document. Available at https://www.ctu.cz/sites/default/files/cs/download/oznamene_typy_rozhrani/orbcomm-rozhrani_02_06_2010.pdf.

[29] Mathworks Charles Rino. Satellite orbit computation. Available at: https://www.mathworks.com/matlabcentral/fileexchange/28888-satellite-orbit-computation.

[30] Mathworks. geodetic2aer documentation. Available at: https://www.mathworks.com/help/map/ref/geodetic2aer.html.

[31] Mathworks. aer2geodetic documentation. Available at: https://www.mathworks.com/help/map/ref/aer2geodetic.html.

[32] Yao-Cheng Lin. Remote sensing of soil moisture with signals of opportunity (soop). Purdue University, 2017. Available at https://docs.lib.purdue.edu/dissertations/AAI10638376/.

[33] Nereida Rodriguez-Alvarez, Xavier Bosch-Lluis, Adriano Camps, Mercè Vall-Llossera, Enric Valencia, Juan Fernando Marchan-Hernandez, and Isaac Ramos-Perez. Soil moisture retrieval using gnss-r techniques: Experimental results over a bare soil field. *IEEE Transactions on Geoscience and Remote Sensing*, 47(11):3616–3624, 2009.

[34] Alberto Alonso-Arroyo, Adriano Camps, Albert Aguasca, Giuseppe Forte, Alessandra Monerris, Christoph Ruediger, Jeffrey P Walker, Hyuk Park, Daniel Pascual, and Raul Onrubia. Improving the accuracy of soil moisture retrievals using the phase difference of the dual-polarization gnss-r interference patterns. *IEEE Geoscience and Remote Sensing Letters*, 11(12):2090–2094, 2014.

[35] ORBCOMM. Orbcomm og2 network. Available at: https://www.orbcomm.com/en/networks/satellite/orbcomm-og2.

[36] ORBCOMM. Orbcomm announces commercial service for its final 11 og2 satellites. Available at: https://www.orbcomm.com/en/company-investors/news/2016/orbcomm-announces-commercial-service-for-its-final-11-og2-satellites.

# APPENDICES

# A. FRONT-END BILL OF MATERIALS

Table A.1.: Bill of Materials

| Item | Quantity | Manufacturer | Model Number | Description |
|---|---|---|---|---|
| 1 | 2 | McMaster Carr | 89015K12 | 12”x12” 6061 Aluminum Sheet, 0.04” thick |
| 2 | 4 | McMaster Carr | 89015K12 | 12”x4” 6061 Aluminum Sheet, 0.04” thick |
| 3 | 8 | McMaster Carr | 1959N14 | Miniature T-Slotted Framing, 10mmx10mmx12” |
| 4 | 4 | McMaster Carr | 1959N11 | Miniature T-Slotted Framing, 10mmx10mmx3” |
| 5 | 8 | McMaster Carr | 1959N55 | 3-Way Outside Corner Bracket, T-Slotted |
| 6 | 2 | Mini Circuits | ZX80-DR230-S+ | Absorptive Switch |
| 7 | 2 | Mini Circuits | ZSW2-63DR+ | Reflective Switch |
| 8 | 6 | Mini Circuits | ZX60-P103LN+ | Low Noise Amplifier |
| 9 | 3 | Omega | SA1-RTD | RTD Temperature Sensor |
| 10 | 2 | Mini Circuits | ZMDC-10-1+ | Directional Coupler |
| 11 | 1 | Mini Circuits | ZFSC-2-372-S+ | Power Splitter |
| 12 | 1 | Pasternack | PE85N1003 | Noise Injection Diode |
| 13 | 2 | Mini Circuits | ZAPB-141-S+ | Band-Pass Filter |
| 14 | 4 | L-Comm | BTS5M | 50 Ohm SMA Terminator |
| 15 | 1 | Ettus | E-310 | USRP Software Defined Radio |
| 16 | 3 | LP/Amazon | B07RNNGHQQ | 9V, 600mAh Rechargable Battery |
| 17 | 1 | Tattu/Amazon | B0728B9T7K | 7.4V, 1000mAh LiPo Battery |
| 18 | 1 | Sparkfun | AST-CAN485 | Arduino Microcontroller |

# B. SOIL MOISTURE RETRIEVAL ALGORITHMS

Soil moisture can be estimated using numerous methods, each with their own advantages and disadvantages. The main methods discussed are the cross-correlation method along with a number of interferometric or phase-based measurements.

## B.1 Expanded Through State Correlations

To give a better idea of using the through state correlations for soil moisture retrieval, the full equations are shown below.

$$X_1(t) = \sqrt{G_1}(\sqrt{G_{AS}(\theta_{DS})}X_D(t)+\sqrt{G_{AS}(\theta_{RS})}X_R(t)+\eta_{AS}+\eta_1+\eta_{Dio})e^{j(\omega_I+\omega_c)t} \quad \text{(B.1)}$$

$$X_2(t) = \sqrt{G_2}(\sqrt{G_{AE}}(\theta_{DE})X_D(t) + \sqrt{G_{AE}}(\theta_{RE})X_R(t) + \eta_{AE} + \eta_2 + \eta_{Dio})e^{j(\omega_I+\omega_c)t} \quad \text{(B.2)}$$

Expanding the correlations to show the components:

$$\begin{aligned} R_{11t}(\tau) = G_1[&C_D(R_s(\tau)e^{j(\omega_I+\omega_c)\tau}(G_{AS}(\theta_{DS}) + G_{AS}(\theta_{RS})\Gamma) \\ &+ \sqrt{G_{AS}(\theta_{DS})G_{AS}(\theta_{RS})\Gamma}(R_s(\tau-\tau_{RD})e^{j(\omega_I+\omega_c)(\tau-\tau_{RD})} \\ &+ R_s(\tau+\tau_{RD})e^{j(\omega_I+\omega_c)(\tau+\tau_{RD})} + kBsinc(B\tau)(T_{AS}+T_1+T_{Dio})] \end{aligned} \quad \text{(B.3)}$$

$$\begin{aligned} R_{22t}(\tau) = G_2[&C_D(R_s(\tau)e^{j(\omega_I+\omega_c)\tau}(G_{AE}(\theta_{DE}) + G_{AE}(\theta_{RE})\Gamma) \\ &+ \sqrt{G_{AE}(\theta_{DE})G_{AE}(\theta_{RE})\Gamma}(R_s(\tau-\tau_{RD})e^{j(\omega_I+\omega_c)(\tau-\tau_{RD})} \\ &+ R_s(\tau+\tau_{RD})e^{j(\omega_I+\omega_c)(\tau+\tau_{RD})})) + kBsinc(B\tau)(T_{AE}+T_2+T_{Dio})] \end{aligned} \quad \text{(B.4)}$$

$$R_{12t}(\tau) = \sqrt{G_1 G_2}[C_D(R_s(\tau)e^{j(\omega_c+\omega_I)\tau}(\sqrt{G_{AS}(\theta_{DS})G_{AE}(\theta_{DE})} + \Gamma\sqrt{G_{AS}(\theta_{RS})G_{AE}(\theta_{RE})}) + \sqrt{G_{AS}(\theta_{DS})G_{AE}(\theta_{RE})}\Gamma R_s(\tau-\tau_{RD})e^{j(\omega_I+\omega_c)(\tau-\tau_{RD})} + \sqrt{G_{AS}(\theta_{RS})G_{AE}(\theta_{DE})}\Gamma R_s(\tau+\tau_{RD})e^{j(\omega_I+\omega_c)(\tau+\tau_{RD})}) + kBT_{Dio}sinc(B\tau)] \quad \text{(B.5)}$$

The reflectivity, $\Gamma$, is present in all of the equations with various other unknowns. To facilitate the retrieval of $\Gamma$, the system and antenna gains $G$, noise temperatures $T$, and signal power $C_D$ must be found. The noise diode temperature $T_{Dio}$ and bandwidth $B$ are known.

An ideal case for this experiment would be to have isolated antennas, where the direct signal is only received by sky antenna and the reflected signal is only received by the Earth antenna. Assuming isolation would simplify the signals to:

$$X_1(t) = \sqrt{G_1}(\sqrt{G_{AS}(\theta_{DS})}X_D(t) + \eta_{AS} + \eta_1 + \eta_{Dio})e^{j(\omega_I+\omega_c)t} \quad \text{(B.6)}$$

$$X_2(t) = \sqrt{G_2}(\sqrt{G_{AE}(\theta_{RE})}X_R(t) + \eta_{AE} + \eta_2 + \eta_{Dio})e^{j(\omega_I+\omega_c)t} \quad \text{(B.7)}$$

with correlations of:

$$R_{11_T}(\tau) = G_1\Big(C_D R_s(\tau)e^{j(\omega_c(\tau)+\omega_I(\tau))}G_{AS}(\theta_{DS}) + kBsinc(B\tau)(T_{AS}+T_1+T_{Dio})\Big) \quad \text{(B.8)}$$

$$R_{22_T}(\tau) = G_2\Big(C_D R_s(\tau)e^{j(\omega_c(\tau)+\omega_I(\tau))}G_{AE}(\theta_{RE})\Gamma + kBsinc(B\tau)(T_{AE}+T_2+T_{Dio})\Big) \quad \text{(B.9)}$$

$$R_{12_T}(\tau) = \sqrt{G_1 G_2}\Bigg( C_D R_s(\tau - \tau_{RD}) e^{j((\omega_c+\omega_I)(\tau-\tau_{RD})+\phi_{RD}))} \sqrt{G_{AS}(\theta_{DS}) G_{AE}(\theta_{RE})\Gamma} + kBsinc(B\tau)(T_{Dio}) \Bigg) \quad \text{(B.10)}$$

While this situation is not realized for this project, it is included to showcase the effects isolation has on calibration and reflectivity retrieval. The correlations become more straightforward and there are fewer unknowns to calibrate for. In addition, reflectivity is only contained in channel 2 since the sky antenna does not receive the reflected signal.

## B.2 Power Measurements

A method based on the correlation equations similar to the example shown in Chapter 2 is possible but difficult given non-isolation. The algorithm is as follows:

Solving for $C_D$ from each equation in the through state:

$$C_D = \frac{R_{11t} - G_1 Q(T_{AS} + T_1 + T_{Dio})}{G_1(R_S(\tau) I\Gamma + H\sqrt{\Gamma}(R_S(\tau - \tau_{RD}) + R_S(\tau + \tau_{RD})))} \quad \text{(B.11)}$$

$$C_D = \frac{R_{22t} - G_2 Q(T_{AE} + T_2 + T_{Dio})}{G_2(R_S(\tau) E\Gamma + F\sqrt{\Gamma}(R_S(\tau - \tau_{RD}) + R_S(\tau + \tau_{RD})))} \quad \text{(B.12)}$$

$$C_D = \frac{R_{12t} - \sqrt{G_1 G_2} Q T_{Dio}}{\sqrt{G_1 G_2}(R_S(\tau)(A + B\Gamma) + \sqrt{\Gamma}(C R_S(\tau - \tau_{RD}) + D R_S(\tau + \tau_{RD})))} \quad \text{(B.13)}$$

where:

$Q = kBsinc(B\tau)$, $A = \sqrt{G_{AS}(\theta_{DS}) G_{AE}(\theta_{DE})}$, $B = \sqrt{G_{AS}(\theta_{RS}) G_{AE}(\theta_{RE})}$,
$C = \sqrt{G_{AS}(\theta_{DS}) G_{AE}(\theta_{RE})}$, $D = \sqrt{G_{AS}(\theta_{RS}) G_{AE}(\theta_{DE})}$, $E = (G_{AE}(\theta_{DE}) + G_{AE}(\theta_{RE}))$,

$F = \sqrt{G_{AE}(\theta_{DE})G_{AE}(\theta_{RE})}$, $I = (G_{AS}(\theta_{DS}) + G_{AS}(\theta_{RS}))$, $H = \sqrt{(G_{AS}(\theta_{DS}) + G_{AS}(\theta_{RS}))}$

By setting two of the equations equal, one can cross multiply and rearrange to find an expression for gamma, albeit in terms of one of the antenna noise temperatures. For example, setting Equations D.1 and D.3 together and rearranging:

$$\Gamma = \frac{G_1 H(R_S(\tau - \tau_{RD}) + R_S(\tau + \tau_{RD}))(R_{12t}(\tau) - \sqrt{G_1 G_2}QT_{Dio})}{R_S(\tau)(\sqrt{G_1 G_2}B(R_{11t} - G_1 Q(T_{AS} + T_1 + T_{Dio})) - G_1 I(R_{12t} - \sqrt{G_1 G_2}QT_{Dio}))} - \frac{\sqrt{G_1 G_2}(CR_S(\tau - \tau_{RD}) + DR_S(\tau + \tau_{RD}))(R_{11t}(\tau) - G_1 Q(T_{AS} + T_1 + T_{Dio}))}{R_S(\tau)(\sqrt{G_1 G_2}B(R_{11t} - G_1 Q(T_{AS} + T_1 + T_{Dio})) - G_1 I(R_{12t} - \sqrt{G_1 G_2}QT_{Dio}))} \tag{B.14}$$

### B.3 Interferometric/Phase Measurements

Interferometry is a technique for obtaining measurements based on the superposition of two waves. That is, through analyzing how two waves constructively and destructively interfere with one another. Superposition and interference can occur in a number of ways, one of which is a change in path length of the wave. Because the system modeled here is composed of a moving UAV and satellites in low Earth orbit, the paths of the signals will change rapidly. This allows for an interferometric, or phase, measurement to be made.

If the gain pattern of an antenna is shaped such that it ends up receiving both the direct and reflected signal, the antennas are said to be non-isolated. This further complicates finding reflectivity, as both antennas will receive part of the component that contains the measurement. In such a case, interferometric measurements based on phase can be used to find reflectivity and soil moisture.

### B.3.1 Least Squares Method

A Least-Squares Approach has been shown to be applicable for phase measurements [32]. Adapting Equation 2.77 as a function of reflectivity and elevation angle:

$$f(\Gamma,\phi)=\frac{(\sqrt{I_E}+\sqrt{I_S}\Gamma)R_{11_T}(\tau_{RD})+\sqrt{\Gamma}R_{11_T}(0)e^{j\phi}+\sqrt{I_SI_E\Gamma}R_{11_T}(2\tau_{RD})e^{-j\phi}}{(1+I_S)\Gamma R_{11_T}(0)+2\sqrt{I_S\Gamma}R_{11_T}(\tau_{RD})\cos(\phi)} \tag{B.15}$$

where $I$ denotes the antenna isolation:

$$I_S=\frac{G_{RS}}{G_{DS}} \tag{B.16}$$

$$I_E=\frac{G_{DE}}{G_{RE}} \tag{B.17}$$

and phase is defined as:

$$\phi=\omega_c\tau_{RD} \tag{B.18}$$

This results in a complex function that can be split into its separate real and imaginary components:

$$f_{Re}(\Gamma,\phi)=\frac{(\sqrt{I_E}+\sqrt{I_S}\Gamma)R_{11_T}(\tau_{RD})+(\sqrt{\Gamma}R_{11_T}(0)+\sqrt{I_SI_E\Gamma}R_{11_T}(2\tau_{RD}))\cos\phi}{(1+I_S)\Gamma R_{11_T}(0)+2\sqrt{I_S\Gamma}R_{11_T}(\tau_{RD})\cos(\phi)} \tag{B.19}$$

$$f_{Im}(\Gamma,\phi)=\frac{(\sqrt{\Gamma}R_{11_T}(0)-\sqrt{I_SI_E\Gamma}R_{11_T}(2\tau_{RD})\sin\phi)}{(1+I_S)\Gamma R_{11_T}(0)+2\sqrt{I_S\Gamma}R_{11_T}(\tau_{RD})\cos(\phi)} \tag{B.20}$$

From these equations, reflectivity can be estimated through iteration using a least squares approximation. The effects of non-isolation on the measurement, based on Equations B.19 and B.20, is shown in Figure B.1 where black represents isolated gain and green represents non-isolated gain, modeled with $G_{RS}=1.865$ dB, $G_{DS}=2.322$ dB, $G_{DE}=1.2372$ dB, and $G_{RE}=5.5124$ dB.

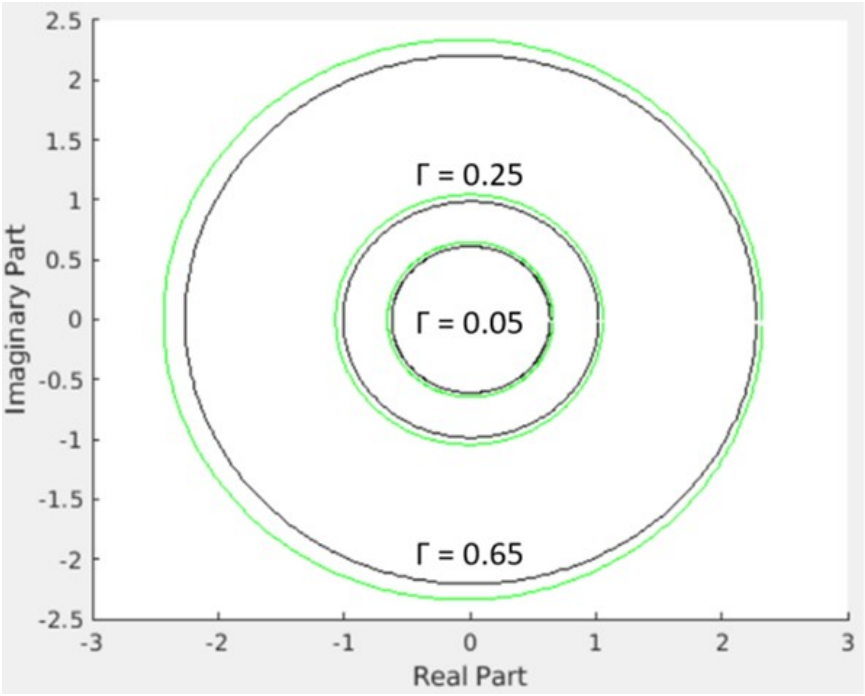


Figure B.1.: Isolated vs Non-Isolated Antennas

At smaller reflectivity, Γ, the effects are harder to notice but as reflectivity increases, the oblong shape effects from the non-isolated gain pattern becomes apparent in the simulated measurement.

### B.3.2 Brewster Angle/IPT Method

Soil moisture can be inferred using the Brewster angle of a signal's phase measurements. A Brewster angle is defined as the angle at which incident EM radiation, with a specific polarization, will pass through a dielectric surface without reflection. Mathematically, it is expressed as a function of the refractive indices of the medium being transmitted:

$$\theta_B = \arctan\left(\frac{n_2}{n_1}\right) \tag{B.21}$$

The method for finding soil moisture is referred to as the dual polarization inter-

ference path technique (IPT) and has been demonstrated before using GPS [33] [34]. IPT uses a linearly polarized antenna to collect both the direct and reflected signals in vertical and horizontal polarizations. By coherently adding the interference patterns at both polarizations, an overall interference pattern is created with a higher frequency component related to the multipath and a lower frequency component related to the antenna. Breaking it down, one obtains received signal power as a sum of the direct and reflected components:

$$P_R \, \alpha \, |E_D + E_R|^2 = F_n(\theta)(1 + |R_q(\theta, \epsilon_r)|e^{j(\Delta\phi + \varphi_q(\theta, \epsilon_r))})^2 \tag{B.22}$$

where $F_n(\theta)$ represents the antenna pattern as a function of incidence angle $\theta$, $E$ represents the electric field, $|R_q(\theta, \epsilon_r)|$ represents the absolute value of the Fresnel reflection coefficient for polarization $q$, $\Delta\phi$ represents the signal multipath phase difference, and $\varphi_q(\theta, \epsilon_r)$ represents the phase of the reflection coefficient at polarization $q$.

Because the phase from multipath can be defined as a function of wavelength and satellite/receiver geometry:

$$\Delta\phi = \left(\frac{4\pi}{\lambda}\right) h \cos(\theta) \tag{B.23}$$

it is independent of wave polarization and thus unsuitable for finding soil moisture. The reflection coefficient phase, however, is polarization dependent making it a key for soil moisture.

Equation B.22 can be simplified further by deriving the overall reflection coefficent term based on an iterative soil layer model. The model described here uses three-layers, one air and two soil layers [33] [34]. As such, the reflection term is defined as:

$$R = e^{-(\frac{4\pi\sigma}{\lambda})} \frac{r_{1,2} + r_{2,3}e^{S}e^{j2\varphi}}{1 + r_{1,2}r_{2,3}e^{S}e^{j2\varphi}} \tag{B.24}$$

where $r$ is the Fresnel reflection coefficient based off of the dielectric constants of two layers and polarization, and $S$ represents the surface roughness correction factor

based on the RMS surface roughness $\sigma$. The reflection coefficient phase, $\varphi$, is defined as a function of layer thickness, $t$, dielectric constant, and incidence angle:

$$\varphi = \frac{2\pi}{\lambda} t_2 \sqrt{\epsilon_{r_2} - \epsilon_{r_1} \sin(\theta)^2} \tag{B.25}$$

Using Equations B.24 and B.25, the IPT power is simplified to:

$$P_R \; \alpha \; F_n(\theta) |1 + R_q e^{j\Delta\phi}|^2 \tag{B.26}$$

To find soil moisture, the IPT of the horizontal and vertical polarizations are calculated and plotted as a function of elevation angle ($90° - \theta_{Inc}$). The elevation angle at which the IPT phase difference between the two polarizations reaches 90 degrees is the Brewster angle. Using Equation B.21, the Brewster angle directly relates to the refractive index of the soil and can allow for a soil moisture map to be made. A simulation of this model is shown in Figure B.2.

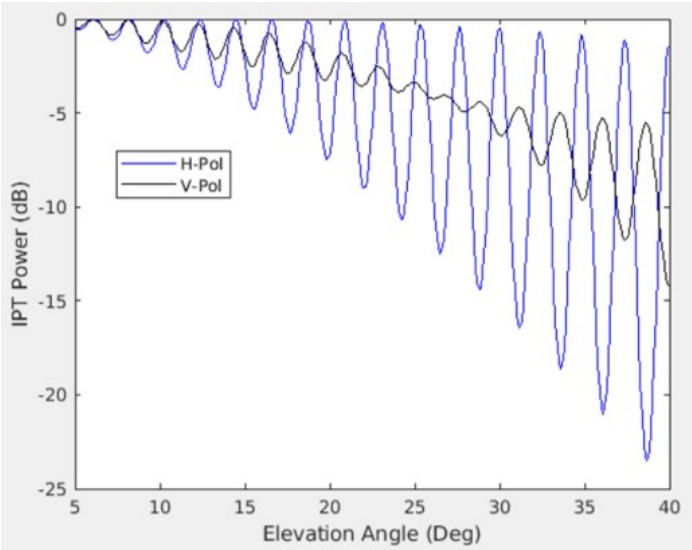


(a) IPT Power 5% Soil Moisture

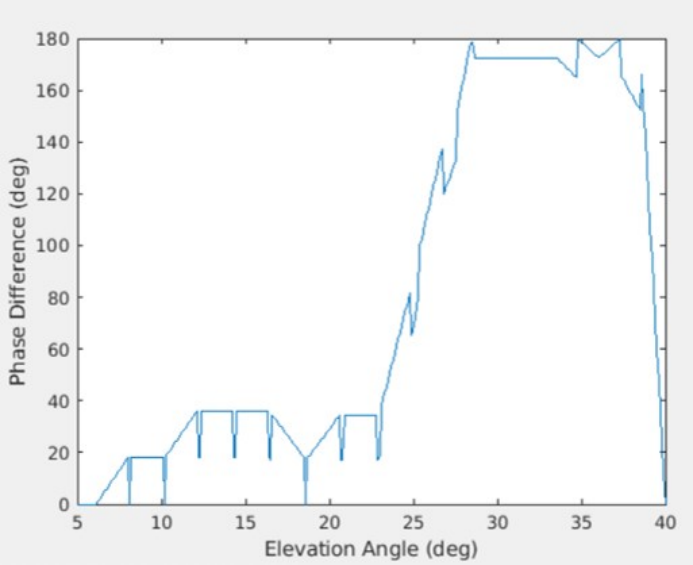


(b) Phase Difference between Polarizations

Figure B.2.: IPT Brewster Angle Simulation

The Brewster angle occurs where the phase difference reaches 90 degrees, which also corresponds to the squished V-Pol amplitude in Figure B.2a. This simulation shows a Brewster angle at roughly 25 degrees. This matches the 5% soil moisture that was used to create the simulation. The jagged lines are the result of discretizing the H-Pol and V-Pol phases in order to find the phase difference. While this does

result in a crude plot, it still shows the basic idea of the method.

It must be noted that this method was designed for use with GPS and L-band, which does not penetrate as far as I or P-band. Because I-band penetrates further, it would hit more refractive layers than an L-band signal and would require a more complicated model.

# C. ORBCOMM SIGNAL PROPERTIES

The hardware design of this project is predicated on the use of ORBCOMM digital communications in the I-Band frequency range. ORBCOMM is a commercial communication provider that focuses on industrial Internet of things (IoT) and machine-to-machine (M2M) telecommunications [35]. The ORBCOMM network consists of an 11 satellite constellation in low-earth orbit (LEO) [36]. The satellites' downlink operates over 12 channels between 137 and 138 MHz, with each channel having 25 KHz of bandwidth [28]. 50 KHz of the overall bandwidth is saved for ORBCOMM gateway purposes. All signals are RHCP. Table C.1 shows the frequencies used by each available channel [28].

Table C.1.: ORBCOMM Channel Frequencies

| **Channel** | **Center Frequency (MHz)** |
|---|---|
| 1 | 137.2000 |
| 2 | 137.2250 |
| 3 | 137.2500 |
| 4 | 137.4400 |
| 5 | 137.4600 |
| 6 | 137.6625 |
| 7 | 137.6875 |
| 8 | 137.7125 |
| 9 | 137.7375 |
| 10 | 137.8000 |
| 11 | 137.2875 |
| 12 | 137.3125 |

# D. BREWSTER ANGLE SIMULATOR MATLAB CODE

```
%% Brewter Angle Simulator
% Jared D. Covert, Purdue AAE, AFIT/CIP
% 05 April 2020
%
% Code for simulating the IPT of H and V-Pol for Brewster angle calcs and
% interferometric measurments for soil moisture
%
% Assume 2 soil layers and air for this model, see Alonso-Arroyo and
% Rodriguez-Alvarez papers
%%%%%%%%%%%%%%%%%%%%%%%%%%%%%%%%%%%%%%%%%%%%%%%%%%%%%%%%%%%%%%%%%%%%%%%%%%%%
%% Generate IPT
% Define constants
f = 137.5e6; % ORBCOMM
lambda = (3e8)/f;
mv1 = .05*1.2; % Assume total soil density of 1.2g/cm^3, 5% soil moisture
mv2 = .20*1.2; % Assume 20% soil moisture for second soil layer
Sand = 0.40; % Sand
C = 0.20; % Clay
Silt = 0.40; % Silt
theta = [5:0.1:40]; % Elevation angle, degrees
theta_inc = 90-theta; % Angle of incidence
t = 0.10; % Thickness of first soil layer, assume possible I-band penetration depth
sigma = 0.05; % RMS surface roughness/height, assume 5 cm
HPBW = 45; % Degrees, assumed
h = 30.48; % Meters, receiver height, assume approx 100 ft

% Calculate soil dielectric constants
epsilon_air = 1; % Assume dielectric air is one, 1st layer
epsilon_soil1 = dielectricmodel(Sand,C,mv1,f); % 2nd layer, 1st soil layer
epsilon_soil2 = dielectricmodel(Sand,C,mv2,f); % 3rd layer, 2nd soil layer
```

```
31
32 % Compute surface roughness correction
33 sigmal = 0.01; % STD soil roughness between layers, assume 1 cm
34 S = -8*((pi*sigmal/lambda)*sqrt(epsilon_soil1-epsilon_air*(sind(theta_inc).^2)));
35
36 % Compute Fresnel coefficients
37 rh12 = (sqrt(epsilon_air-epsilon_air.*(sind(theta_inc).^2))-...
38     sqrt(epsilon_soil1-epsilon_air.*(sind(theta_inc).^2))./...
39     (sqrt(epsilon_air-epsilon_air.*(sind(theta_inc).^2))+...
40     sqrt(epsilon_soil1-epsilon_air.*(sind(theta_inc).^2)));
41
42 rh23 = (sqrt(epsilon_soil1-epsilon_soil1.*(sind(theta_inc).^2))-...
43     sqrt(epsilon_soil2-epsilon_soil1.*(sind(theta_inc).^2))./...
44     (sqrt(epsilon_soil1-epsilon_soil1.*(sind(theta_inc).^2))+...
45     sqrt(epsilon_soil2-epsilon_soil1.*(sind(theta_inc).^2)));
46
47 rv12 = (epsilon_soil1*sqrt(epsilon_air-epsilon_air.*(sind(theta_inc).^2))-...
48     epsilon_air*sqrt(epsilon_soil1-epsilon_air.*(sind(theta_inc).^2)))./...
49     (epsilon_soil1*sqrt(epsilon_air-epsilon_air.*(sind(theta_inc).^2))+...
50     epsilon_air*sqrt(epsilon_soil1-epsilon_air.*(sind(theta_inc).^2)));
51
52 rv23 = (epsilon_soil2*sqrt(epsilon_soil1-epsilon_soil1.*(sind(theta_inc).^2))-...
53     epsilon_soil1*sqrt(epsilon_soil2-epsilon_soil1.*(sind(theta_inc).^2)))./...
54     (epsilon_soil2*sqrt(epsilon_soil1-epsilon_soil1.*(sind(theta_inc).^2))+...
55     epsilon_soil1*sqrt(epsilon_soil2-epsilon_soil1.*(sind(theta_inc).^2)));
56
57 % Compute reflection coefficient phase
58 rphase = (2*pi/lambda)*t*sqrt(epsilon_soil1-epsilon_air.*(sind(theta_inc).^2));
59
60 % Compute overall reflection term
61 Rh = exp(-((4*pi*sigma)/lambda)^2)*((rh12+rh23.*exp(S).*exp(j.*2.*rphase))./...
62     (1+rh12.*rh23.*exp(S).*exp(j.*2.*rphase)));
63
64 Rv = exp(-((4*pi*sigma)/lambda)^2)*((rv12+rv23.*exp(S).*exp(j.*2.*rphase))./...
65     (1+rv12.*rv23.*exp(S).*exp(j.*2.*rphase)));
```

```
% determine the phase difference
% at the maximum point.
% Estimate antenna radiation pattern (only used for magnitude if IPT,
% complete accuracy not required)
F = -12*(theta/HPBW).^2; % in dB

% Calculate signal multipath phase difference
deltaphi = (4*pi/lambda)*h*cosd(theta_inc);

% Compute IPT Power
Ph = F.*abs(1+Rh.*exp(j*deltaphi)).^2;
Pv = F.*abs(1+Rv.*exp(j*deltaphi)).^2;

% Plot
figure(1)
plot(theta,Ph,'b')
hold on
plot(theta,Pv,'k')
xlabel('Elevation Angle (Deg)')
ylabel('IPT Power (dB)')

%% Calculate Phase Difference

% Calculate horizontal phase
[X,loc1] = findpeaks(Ph);
hphase = zeros(length(Ph)-loc1(1),1);
counter2 = 0;

for counter = 1:length(loc1)-1
    A = loc1(counter+1);
    B = loc1(counter);
     if counter == 1
      hphase(1:A-B) = linspace(0,360,A-B);
     else
      hphase(counter2+1:counter2+(A-B)) = linspace(0,360,A-B);
```

```
101       end
102       counter2 = counter2 + (A-B);  % Placekeeper for position along sinusoid
103  end
104  hphase = [zeros(loc1(1)-1,1);hphase;1];
105  hphase(A:length(hphase)) = linspace(0,360,length(hphase)-A+1);
106
107  % Calculate vertical phase
108  [Y,loc2] = findpeaks(Pv);
109  vphase = zeros(length(Pv)-loc2(1),1);
110  counter2 = 0;
111
112  for counter = 1:length(loc2)-1
113      A = loc2(counter+1);
114      B = loc2(counter);
115       if counter == 1
116        vphase(1:A-B) = linspace(0,360,A-B);
117       else
118        vphase(counter2+1:counter2+(A-B)) = linspace(0,360,A-B);
119       end
120       counter2 = counter2 + (A-B);  % Placekeeper for position along sinusoid
121  end
122  vphase = [zeros(loc2(1)-1,1);vphase;1];
123  vphase(A:length(vphase)) = linspace(0,360,length(vphase)-A+1);
124
125
126  % Find difference
127  phasediff = abs(vphase-hphase);
128
129  % Correction for phase of 360
130   for n = 1:length(phasediff)
131        if abs(phasediff(n))>180
132            phasediff(n) = 360-phasediff(n);
133        else
134        end
135    end
```

```
136   figure(2)
137   plot(theta,phasediff)
138   xlabel('Elevation Angle (deg)')
139   ylabel('Phase Difference (deg)')
```

# E. ISOLATION PATTERN SIMULATOR MATLAB CODE

```
%% Interference/Phase Code for Reflectivity
% Jared Covert, AFIT/CIP, Purdue AAE
% 27 February 2020
%%%%%%%%%%%%%%%%%%%%%%%%%%%%%%%%%%%%%%%%%%%%%%%%%%%%%%%%%%%%%%%%%%%%%%%%%%%%
% Define constants and parameters
% Antennas have omin-directional gain
G_SD = 1;
G_SR = 1;
G_ED = 1;
G_ER = 1;
I_S = G_SR/G_SD; % Both isolation terms are one due to omni-directional, non-isolation
I_E = G_ED/G_ER;
R_a0 = 4e-13; % Autocorrelation at t=0
Ra_Trd = 6e-15; % Auto at tauRD
Ra_TTrd = 6e-15; % Auto at 2tauRD
gamma = [0.05; 0.25; 0.65]; % reflectivity
phase = [0:1:359]'; % phase in degrees

% Calculate real and imaginary parts
real = ones(360,3);
imag = ones(360,3);

for n = 1:3
    real(:,n) = ((sqrt(I_E)+sqrt(I_S)*gamma(n))*Ra_Trd+(sqrt(gamma(n))*R_a0+sqrt(I_S*I_E*gamma(n))*Ra_TTrd)...
          *cosd(phase))./(((1+I_S)*gamma(n))*R_a0+2*sqrt(I_S*gamma(n))*Ra_Trd*cosd(phase));

    imag(:,n) = ((sqrt(gamma(n))*R_a0-sqrt(I_S*I_E*gamma(n))*Ra_TTrd)*sind(phase))...
        ./(((1+I_S)*gamma(n))*R_a0+2*sqrt(I_S*gamma(n))*Ra_Trd*cosd(phase));
end

% Plot
hold on
plot(real(:,1),imag(:,1),'k')
plot(real(:,2),imag(:,2),'k')
plot(real(:,3),imag(:,3),'k')
xL =  xlim;
yL = ylim;

%% Non-Isolation
G_SD = 10^(2.3222/10);
G_SR = 10^(1.865/10);
G_ED = 10^(1.2372/10);
G_ER = 10^(5.5124/10);
I_S = G_SR/G_SD; % Both isolation terms are one due to omni-directional, non-isolation
I_E = G_ED/G_ER;
R_a0 = 4e-13; % Autocorrelation at t=0
Ra_Trd = 6e-15; % Auto at tauRD
Ra_TTrd = 6e-15; % Auto at 2tauRD
gamma = [0.05; 0.25; 0.65]; % reflectivity
phase = [0:1:359]'; % phase in degrees

% Calculate real and imaginary parts
```

```
real = ones(360,3);
imag = ones(360,3);

for n = 1:3
    real(:,n) = ((sqrt(I_E)+sqrt(I_S)*gamma(n))*Ra_Trd+(sqrt(gamma(n))*R_a0+sqrt(I_S*I_E*gamma(n))*Ra_TTrd)...
          *cosd(phase))./(((1+I_S)*gamma(n))*R_a0+2*sqrt(I_S*gamma(n))*Ra_Trd*cosd(phase));

    imag(:,n) = ((sqrt(gamma(n))*R_a0-sqrt(I_S*I_E*gamma(n))*Ra_TTrd)*sind(phase))...
        ./(((1+I_S)*gamma(n))*R_a0+2*sqrt(I_S*gamma(n))*Ra_Trd*cosd(phase));
end


plot(real(:,1),imag(:,1),'g')
plot(real(:,2),imag(:,2),'g')
plot(real(:,3),imag(:,3),'g')

xlabel('Real Part')
ylabel('Imaginary Part')

```

# F. SPECULAR POINT MAPPING MATLAB CODE

```
%% Specular Point Mapping Code
% Calculation of satellite position from TLE and mapping of specular points
% based on reference location. Code also creates a KML file for overlaying
% the specular points and field in Google Earth
%
%
% Original Author: Zenki
% Modified: 2d LT Jared Covert, Purdue AAE, AFIT/CIP
% Last Modified: 15 Apr 2019
%
% Includes Google earth toolbox (gearth_lib)
% and SPG4 toolbox from Matlab website (orbit_lib)
%
% AER: Azimuth, Elevation, Slant distance
% LLH: Latitude, Longtitude, Height
%
% Globals: None
%
% Coupling: Folders orbit and googleearth
%%%%%%%%%%%%%%%%%%%%%%%%%%%%%%%%%%%%%%%%%%%%%%%%%%%%%%%%%%%%%%%%%%%%%%%%%%%%

clear all;
close all;
clc;
gearth_lib = './googleearth/';
orbit_lib = './orbit/';

% Select satellite system, load the corresponding satellite system
% and save kml file with the same name in the end
% Orbcomm
% Weather satellite
% UFO
% MUOS
% SBAS
% XM

% ============Satelite system========
sat_name  = ['orbcomm'];
tle_file  = [sat_name '.tle'];


addpath(gearth_lib);
addpath(orbit_lib);
%=============Inputs=============
%%
% 2018 Tower location, reference for field location, deg
tlat = 40.474418;
tlon = -86.991783;

% Frequency for different systems
freq            = 137.5e+6 * strcmp(sat_name, 'orbcomm') +...
                  137.5e+6 * strcmp(sat_name, 'weather') +...
```

```
                    260e+6 * strcmp(sat_name, 'ufo') +...
                    370e+6 * strcmp(sat_name, 'muos') +...
                    1575.42e+6 * strcmp(sat_name, 'sbas') +...
                    2342.205e+6 * strcmp(sat_name, 'xm');
c                = 299792458;  % Speed of light in m/s
c_tau            = c/freq;

% Angle for elliptic area of Fresnel zone
f_pt             = (0:0.01:1)*2*pi;

sky_mask         = 10;         % cutoff elevation angle in deg    -Is this too low??, ask Garrison
% %% Use this input to get from time and GPS file
% % Input from file
% GPSImport.m % This takes from file GPS_dat.text, change inside script if need be
% % Time info
% time = datetime(GPSdat.Time,'InputFormat','"yyyy-MM-dd''T''HH:mm:ss.SSS''Z"');
% yr = time.Year;
% mon = time.Month;
% day = time.Day;
% hr = time.Hour;
% mins = time.Minute;
% sec = time.Second;
% % GPS reference location info
% ref_lat = GPSdat.Lat; % Deg
% ref_lon = GPSdat.Lon; % Deg
% ref_h = GPSdat.Alt; % Altitude (m); FAA max is 400 AGL
% ref_gnd = 187.1472; % Ground above sea level (m)

%% Use this input format below to manually input time and GPS
% Time vector from drone/USRP (UTC, EST+5)
yr = [2019;2019;2019];
mon = [2;2;2];
day = [11;11;11];
hr = [19;19;19];
mins = [30;30;30];
sec = [0;10;20];

% Reference location from USRP
ref_lat          =  [40.4744;40.4744;40.4744]; % Deg
ref_lon          = [-86.9918;-86.9918;-86.9918]; % Deg
ref_h            =  [20;80;110];     % Height above ground (m); 121.92m=400ftAGL is FAA Max
ref_gnd          = 187.1472;   % Ground altitude above sea level (m)

%% Make/plot the field
%%==============Tile Locations
%don't trust the lat_long_old things
lat_old           =  40.474676; % orginally 40.474667
lon_old           = -86.992289;

% lat_tilt1 = [40.474613 40.474618 40.473805 40.473806 40.474613];
% lon_tilt1 = [-86.991385 -86.992841 -86.992842 -86.991387 -86.991385];

% 2 -- 1
% ------
% 3 --- 4
%
lat_tilt1 = [40.474640 40.474642 40.473793  40.473789 40.474640];
lon_tilt1 = [-86.991385 -86.992705  -86.992724 -86.991375 -86.991385];
llh_tilt1 = [lat_tilt1' lon_tilt1' zeros(1,length(lat_tilt1))'];

```

```
113 [tEast,tNorth,tUp] = geodetic2enu(lat_tilt1, lon_tilt1, zeros(1,length(lat_tilt1)),...
114                                   tlat,tlon,0,wgs84Ellipsoid);
115 [xEast,yNorth,zUp] = geodetic2enu(lat_old,lon_old,0,...
116                                   tlat,tlon,0,wgs84Ellipsoid);
117 drainage_E = tEast(1:2);
118 drainage_N(1) = 0 + yNorth;
119 drainage_N(2) = -33.75*0.3048 + yNorth;
120 drainage_N(3) = (-33.75 - 67.5)*0.3048 + yNorth;
121 drainage_N(4) = (-33.75 - 67.5*2)*0.3048 + yNorth;
122 drainage_N(5) = (-33.75 - 67.5*3)*0.3048 + yNorth;
123 drainage_N(6) = (-33.75 - 67.5*4)*0.3048 + yNorth;
124 drainage_N(7) = (-33.75 - 67.5*4 - 18.75)*0.3048 + yNorth;
125
126 figure(1)
127 hold on;
128
129 plot(tEast, tNorth, 'g', 'linewidth',2) % this must plot the field.
130 field_ge_out = ge_plot(lon_tilt1, lat_tilt1,'lineWidth',3,'lineColor','FFEF3E47','name', 'FieldOutline');
131
132
133 [geo_E_1_lat, geo_E_1_lon, temp] = enu2geodetic(drainage_E(1), drainage_N, 0,tlat, tlon, zUp, wgs84Ellipsoid);
134 [geo_E_2_lat, geo_E_2_lon, temp]= enu2geodetic(drainage_E(2), drainage_N, 0,tlat, tlon, zUp, wgs84Ellipsoid);
135 drainageTiles_ge_out = [];
136
137 for index = 1:length(drainage_N)
138     plot(drainage_E, [1 1]* drainage_N(index),'k');
139
140     drainageTiles_ge_out = [drainageTiles_ge_out ge_plot([geo_E_1_lon(index), geo_E_2_lon(index)],[geo_E_1_lat(index), geo_E_2_lat(index)],'
141 end
142
143 %%calc trailer pos
144
145 IntofieldW = (tEast(1)+ tEast(4))/2;
146 IntofieldS = (tNorth(1)+ tNorth(2))/2;
147
148 %% Plot specular points/f zones
149
150 % Initialize KML data matrices outside loop
151 sat_ge_out_kml = [];
152 ref_ge_out_kml = [];
153 box_ge_out_kml = [];
154 specpt_ge_out_kml = [];
155 specptline_ge_out_kml = [];
156
157 for index_t = 1:length(yr) % For each time/position point
158
159 start_day       = jday(yr(index_t),mon(index_t),day(index_t),hr(index_t),mins(index_t),sec(index_t)); % UTC time (EST+5)
160 end_day         = jday(yr(index_t),mon(index_t),day(index_t),hr(index_t),mins(index_t),sec(index_t));
161 int_time        = 60/60/24/2; % 10/n minutes??, irrelecent I believe with how i have it running
162
163 file.jday_vec   = start_day:int_time:end_day;
164
165 [satrec, name]  = tle_loaderv2(tle_file);  % Uses the TLE to calulate various Astro properties
166 satrec          = satpos(satrec, file.jday_vec);
167
168 %%===============
169 %%
170 figure(2);
171 hold on;
172 tw_line = [];
```

```
ar_line = [];
sat_ge_out = [];
ref_ge_out = ge_point(ref_lon(index_t), ref_lat(index_t), 0,'iconURL','http://maps.google.com/mapfiles/kml/shapes/placemark_square.png','des
                                                                    'From North Boundry: ' num2str(IntofieldS) ' (m)' ...
                                                                    'From East Boundry: ' num2str(distdim(IntofieldW,'m','f')) '
                                                                    'From North Boundry: ' num2str(distdim(IntofieldS,'m' ,'ft')
max_lat = [];
max_lon = [];
min_lat = [];
min_lon = [];
perpAngleAz = [];

% Process each satellite
for index_sat = 1:length(satrec) % For each satellite

    % Calculate azimuth, elevation, and slant distance from reference point
    % to satellite
    [az, el, slrange] = geodetic2aer(rad2deg(satrec(index_sat).xsat_llh(1,:)),...
                                     rad2deg(satrec(index_sat).xsat_llh(2,:)),...
                                     satrec(index_sat).xsat_llh(3,:),...
                                     ref_lat(index_t), ref_lon(index_t), ref_h(index_t) + ref_gnd,...
                                     wgs84Ellipsoid);
     % AER: Reference point to satellite
    satrec(index_sat).aer       = [az;el;slrange]; % Setting az,el,range into the satvec struct
     % AER: Ground of reference point to specular point
    satrec(index_sat).spec_aer  = [az;zeros(size(az));ref_h(index_t)./tand(el)];
    % LLH: specular point
    [lat, lon, h]               = aer2geodetic(az, zeros(size(az)), ref_h(index_t)./tand(el),...
                                   ref_lat(index_t), ref_lon(index_t), ref_gnd,...
                                   wgs84Ellipsoid);
    satrec(index_sat).spec_llh  = [lat;lon;h];
    sp_ge_out = [];
%     if sum(el > sky_mask)>0
%         sp_ge_out = ge_point(lon(el > sky_mask),...
%                              lat(el > sky_mask),...
%                              zeros(size(lon(el > sky_mask))));
%     end

    el_mask = sign(el - sky_mask);
    el_cross = find(((el_mask(2:end).*el_mask(1:end-1)))<0);

    %%Determine trailer orientation
    % Trailer is 6.71 meters long
    perpAngleAz(index_sat) = mean(az)+90;


    % Content for KML file - Used for Google Earth
    for index_cross = 1:2:(length(el_cross)-1)
        sp_ge_out = [sp_ge_out ge_plot(lon(el_cross(index_cross)-1: el_cross(index_cross+1)+1),...
                                       lat(el_cross(index_cross)-1: el_cross(index_cross+1)+1),...
                                       'name',char(name{index_sat}))];
    end

    % Fresnel zone
    a = sqrt(ref_h(index_t)*c_tau*sind(el))./(sind(el).^2);
    b = sqrt(ref_h(index_t)*c_tau*sind(el))./sind(el);
    spec_ge_out = [];

    [el_max, el_max_idx] = max(el(el > sky_mask));
    [el_min, el_min_idx] = min(el(el > sky_mask));
```

```
233
234     for index_fr = 1:length(a)
235         if el(index_fr) > sky_mask
236             y = (b(index_fr)*cos(f_pt) + 1j*a(index_fr)*sin(f_pt))*...
237                 exp(-1j*deg2rad(az(index_fr)));
238
239             [lat_y, lon_y, h_y] = enu2geodetic(real(y), imag(y), zeros(size(y)),...
240                                     lat(index_fr), lon(index_fr), h(index_fr), wgs84Ellipsoid);
241
242             % Line from reference point toward specular point
243             tw_line(end+1) = plot([ref_lon(index_t) lon(index_fr)], [ref_lat(index_t) lat(index_fr)], 'rx-');
244             ar_line(end+1) = fill(lon_y, lat_y, 'c','edgecolor','none');
245
246             % Replot the reference points so they stand out
247             plot(ref_lon(index_t),ref_lat(index_t),'bs');
248
249              % This makes specular points for KML
250             specpt_ge_out = ge_point(lon(index_fr),lat(index_fr),h(index_fr),'iconURL','http://maps.google.com/mapfiles/kml/shapes/placemark
251             specpt_ge_out_kml = [specpt_ge_out_kml specpt_ge_out];
252
253             % This makes lines between ref pt to specular pt in KML data
254             specptline_ge_out = ge_gplot([0 1;1 0],[lon(index_fr) lat(index_fr);ref_lon(index_t) ref_lat(index_t)],'lineColor','FF0000FF');
255             specptline_ge_out_kml = [specptline_ge_out_kml specptline_ge_out];
256
257
258             [yeard,mond,dayd,hrd,mind,secd] = invjday (file.jday_vec(index_fr));
259
260 %             if (el(index_fr) == el_max) || (el(index_fr) == el_min)
261                 % KML satellite and fresnal zone content
262                 spec_ge_out = [spec_ge_out ge_poly(lon_y,lat_y,...
263                                 'name',datestr([yeard,mond,dayd,hrd,mind,secd],'yyyy/mm/dd HH:MM'),...
264                                 'lineWidth',1,...
265                                 'polyColor','8FFFFFFF',...
266                                 'description',['EL: ' num2str(el(index_fr)) ' AZ: ' num2str(az(index_fr)) ...
267                                                ])];
268
269 %             end
270
271             max_lat = max([max_lat lat_y]);
272             max_lon = max([max_lon lon_y]);
273             min_lat = min([min_lat lat_y]);
274             min_lon = min([min_lon lon_y]);
275
276         end
277
278     end
279     if sum(el > sky_mask) > 0
280         sat_ge_out = [sat_ge_out ge_folder(char(name{index_sat}), [sp_ge_out ge_folder('Fresnel',spec_ge_out)])];
281     end
282
283
284 end
285
286
287
288 % Generate KML file data for Google earth
289 format long
290 uistack(tw_line(:),'top');
291 axis equal;
292
```

```
293 % This makes stay out box for KML
294 box_lat = [max_lat max_lat min_lat min_lat max_lat];
295 box_lon = [max_lon min_lon min_lon max_lon max_lon];
296 plot(box_lon, box_lat);
297 box_ge_out = ge_poly(box_lon,box_lat,...
298                                 'lineWidth',1,...
299                                 'polyColor','8FFF0000',...
300                                 'description',[' Lon:' num2str(max_lon,'%4.6f') ' ' num2str(min_lon,'%4.6f') ...
301                                                 ' Lat:' num2str(max_lat,'%4.6f') ' ' num2str(min_lat,'%4.6f')]);
302
303 % Create KML file data by adding to old file to add each specular point
304 sat_ge_out_kml = [sat_ge_out_kml sat_ge_out];
305 ref_ge_out_kml = [ref_ge_out_kml ref_ge_out];
306 box_ge_out_kml = [box_ge_out_kml box_ge_out];
307 end
308
309 %Plot trailer, carful I select the first iteration of the loop!
310 %perpAngleAz(1)
311 % tEast,tNorth location in meters of the tower.
312
313 %1--------2
314 %hitch---tower
315 %4--------3
316 cornerN = [];
317 cornerE = [];
318 % Calc rear LH corner of the trailer.
319 cornerN(3) = cosd(mean(az(1,:)))*(0.5*2.57);
320 cornerE(3) = sind(mean(az(1,:)))*(0.5*2.57);
321 % calc rear RH of trailer
322 cornerN(2) = -1*(cosd(mean(az(1,:)))*(0.5*2.57));
323 cornerE(2) =  -1*(sind(mean(az(1,:)))*(0.5*2.57));
324 % calc front Rh trailer
325 cornerN(1) = cornerN(2)+ cosd((mean(az(1,:))+90))*6.71;
326 cornerE(1) = cornerE(2)+ sind((mean(az(1,:))+90))*6.71;
327 % calc front LH trailer
328 cornerN(4) = cornerN(3) + cosd((mean(az(1,:))+90))*6.71;
329 cornerE(4) = cornerE(3) + sind((mean(az(1,:))+90))*6.71;
330
331 % 2.57 trailer width, 6.71 trailer length
332
333 [geoTrailerPosition_lat, geoTrailerPosition_lon] = enu2geodetic(cornerE, cornerN, 0,tlat, tlon, zUp, wgs84Ellipsoid);
334
335 trailer_ge_out = ge_poly(geoTrailerPosition_lon, geoTrailerPosition_lat, 'lineWidth',1,'polyColor','8F10E866',...
336                                         'description',['Trailer Azimuth:' num2str(mean(az(1,:)+90))]);
337
338 % Generate KML file
339 ge_output([sat_name '.kml'],[sat_ge_out_kml ref_ge_out_kml specpt_ge_out_kml specptline_ge_out_kml field_ge_out box_ge_out_kml drainageTiles
340 save([sat_name '.mat'], 'satrec');
341
342 %% Plot Elevation v Time  -this is busted needs fixed, Do i even need this?, i know why its busted
343 % figure(3);
344 % hold on;
345 % for index_sat = 1:length(satrec) % for each satellite
346 %
347 %         plot(file.jday_vec, satrec(index_sat).aer(2,:))
348 %
349 % end
350 % set(gca, 'XTick', file.jday_vec(1):2/24:file.jday_vec(end))
351 % datetick('x','MM');  % This plots the time as minutes
352 % ylabel('Elevation (deg)');grid on;
```

```
353 % title('Time v. Elevation');
```